JGR Solid Earth

Key Points:

- Force balance requires an increase in mountain height when submarine relief is reduced at the subduction-collision transition
- The required increase is several hundred meters to a few kilometers depending mainly on the trench depth and the shear force magnitude
- A delayed increase in mountain height relative to onset of collision increases the upper-plate compression and supports mountain building

Correspondence to:

A. Dielforder,
dielforder@geowi.uni-hannover.de

Force-Balance Analysis of Stress Changes During the Subduction-Collision Transition and Implications for the Rise of Mountain Belts

A. Dielforder[1,2] and **A. Hampel[2]**

[1]GFZ German Research Centre for Geosciences, Potsdam, Germany, [2]Institut für Geologie, Leibniz Universität Hannover, Hannover, Germany

Abstract Mountain height at convergent plate margins is limited by the megathrust shear force, but it remains unclear how this constraint affects the topographic evolution and mountain building at the transition from subduction to collision. Generally, mountain height increases during the subduction-collision transition in response to crustal thickening or processes like mantle delamination and slab breakoff, but the main parameters controlling how much mountain height increases remain poorly understood. Here we show, based on analytical and finite-element force-balance models, that the increase in mountain height depends on the magnitude of the megathrust shear force and the reduction of submarine margin relief. During the subduction stage, the shear force is balanced by the gravitational effect of the margin relief and the deviatoric stresses in the upper plate are low. When the submarine margin relief is reduced during the closure of the ocean basin, the effect of the gravitational force decreases and the upper plate experiences enhanced deviatoric compression, which allows the mountain height to increase until a near-neutral stress state beneath the high mountains is restored. If the increase in mountain height cannot keep pace with the submarine relief reduction, the compression of the upper plate increases by a few tens of MPa, which promotes tectonic shortening and mountain building. Our analysis implies that mountain height can increase by hundreds of meters to a few kilometers during collision, depending primarily on the trench depth during the subduction stage and possible syncollisional changes of the megathrust shear force.

1. Introduction

With the transition from oceanic subduction to continental collision, mountain ranges at convergent plate margins typically experience a phase of surface uplift and an increase in mountain height (Figure 1). For example, stable isotope and paleo-drainage basin analyses indicate that the central European Alps grew in elevation from about 0.3 ± 0.2 km to 1.9 ± 1.0 km between 31 Ma and 22 Ma, and then to 2.9 ± 1.0 km after 15 Ma, suggesting an elevation increase of ≥2 km following the late Eocene subduction-collision transition (Campani et al., 2012; Schlunegger & Kissling, 2015). The collision of Australia's northern passive margin with island arcs of the Pacific plate gave rise to the high mountain ranges of Papua New Guinea and caused up to ∼3 km of surface uplift, as recorded by middle Miocene to Quaternary hemipelagic sediments occurring at modern elevations of ≥2.5 km (Abbott et al., 1997; Abers & McCaffrey, 1994; Baldwin et al., 2012). The rise of the Himalayan orogen since the onset of the India-Asia collision is still controversial, especially with respect to its timing relative to the rise of Tibet (Botsyun et al., 2019; Rowley & Currie, 2006; Saylor et al., 2009; Song et al., 2010; Spicer et al., 2020; Xu et al., 2015). Stable isotope paleoaltimetry data indicate that the Himalaya reached its present elevation by Early Miocene (Gébelin et al., 2013). More recent studies, which also included paleoaltimetric data based on fossil flora, showed that the proto-Himalaya increased from ∼1 km in the late Paleocene to ∼2.3 km at the beginning of the Miocene and reached its present mean elevation by ∼20 Ma (Ding et al., 2017; Xu et al., 2018). An increase in mountain height during the subduction-collision transition has also been inferred for the Central Taiwan orogen, although the absolute change in elevation is not well constrained (e.g., Lee et al., 2006). A present-day margin where a lateral transition from subduction to collision can be observed is the Arabian-Eurasian convergent plate boundary, which exhibits an increase in upper-plate mountain height from the Makran subduction zone in the east to the continental collision zone with the Zagros fold-and-thrust-belt to the west (Mouthereau et al., 2012; Penney et al., 2017).
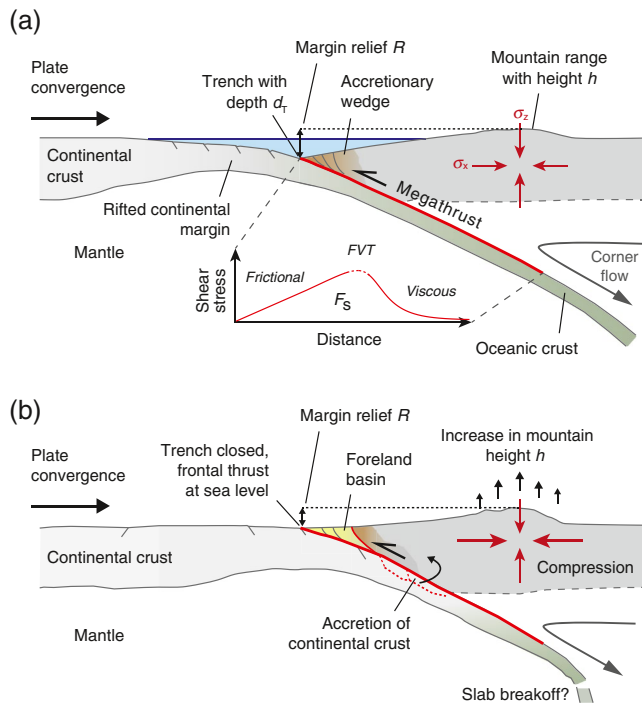
Figure 1. Schematic summary of the subduction-collision transition. (a) Subduction stage. The shear force along the megathrust (F_s) is the integrated shear stress along the fault, comprising an upper frictional segment and a lower viscous segment that merge around the frictional-viscous transition (FVT). The downdip termination of the viscous segment is where temperatures are large enough for viscous shear to occur at low shear stresses. The megathrust shear force balances the gravitational effect of the margin relief, that is, the elevation difference between the trench and height of the mountain range h. If F_s equals the effect of gravity, then the vertical stress σ_z and the horizontal stress σ_x become approximately equal underneath the high mountains. (b) Collision stage. Underthrusting of the continental margin results in the closure of the trench, which reduces the gravitational effect of margin relief and causes enhanced deviatoric compression in the upper plate. As a result, mountain height must increase, which may be driven by accretion, tectonic shortening, and other processes like slab breakoff.

The increase in mountain height during the subduction-collision transition can be understood as an isostatic response of the lithosphere to crustal thickening driven by upper-plate tectonic shortening and accretion of passive margin sediments and crystalline basement units to the orogenic wedge (Dielforder et al., 2016; R. Gao et al., 2016; Garzic et al., 2019; Lamb & Watts, 2010; McIntosh et al., 2013; Molnar & Lyon-Caen, 1988; Rosenberg & Berger, 2009). Continental collision and crustal thickening are also thought to increase the resistance to plate convergence and hence decrease the convergence rate, until collision may eventually cease and convergence is accommodated elsewhere in the plate tectonic system (Cloos, 1993; Copley et al., 2010; Molnar & Stock, 2009; Moores & Twiss, 1995). From this perspective, mountain heights may increase as long as collision and crustal thickening continues, albeit counteracted by erosion. Surface uplift may also be caused by other processes like mantle delamination and breakoff of the subducted oceanic slab, which ultimately trigger an isostatic response (Buiter et al., 2002; Cloos et al., 2005; Duretz et al., 2011; Molnar & Stock, 2009; Sinclair, 1997).

Whatever the actual process that causes surface uplift during the subduction-collision transition may be, it is important to note that the forces that raise the mountains are limited by the maximum force that can be transmitted across the plate boundary (Lamb & Watts, 2010). To evaluate the effect of the shear force along the subduction megathrust against the effects of the gravitational force, force-balance models have been used (Husson & Ricard, 2004; Lamb & Davis, 2003; Seno, 2009; Wang & He, 1999). According to these models, the effect of the gravitational force causes deviatoric tension in the upper plate, whereas the effect of the shear force along the megathrust causes deviatoric compression and supports the upper plate mechanically. Furthermore, it has been argued that the effects of gravity and the megathrust shear force are approximately balanced, with the consequence that the margin relief and thus mountain height is limited by the magnitude of the megathrust shear force (Figure 1; Dielforder, 2017; Lamb, 2006). The approximate balance between the effects of gravity and the shear force implies that the stress state underneath the area of highest elevations is near neutral. Moreover, the stress state may vary locally and temporally between deviatoric compression and deviatoric tension due to small differences in topography and strength of the plate boundary fault (Lamb, 2006; Wang et al., 2019; Wimpenny et al., 2020). A near-neutral upper-plate stress field is also consistent with the observation that faulting in the upper plate can switch from reverse faulting at low elevations to strike-slip and normal faulting at high elevations (e.g., Dalmayrac & Molnar, 1981; Molnar & Lyon-Caen, 1988; Penney et al., 2017). Likewise, the near-neutral stress conditions agree with the finding that fluctuations in megathrust shear stress over the earthquake cycle of a few MPa can cause large rotations of the principal stress axes and change the fault kinematics in the upper plate (e.g., Dielforder et al., 2015; Hardebeck & Okada; 2018; Wang, 2000).

Recently, Dielforder et al. (2020) determined the shear force along active megathrusts worldwide and showed that mountain heights are indeed consistent with an approximate balance between the megathrust shear force and the effects of the gravitational force. This implies that mountain building processes are capable of driving mountain elevations up to the limit imposed by the megathrust shear force irrespective of erosion. The findings of Dielforder et al. (2020) also showed that at subduction zones a considerable portion of the megathrust shear force is needed to support the submarine margin topography, as previously suggested by Lamb (2006). As the transition from subduction to collision is associated with the closure of the ocean basin and a reduction of the submarine margin topography, it can be expected that the effect of the gravitational force changes substantially with the onset of collision. However, the resulting changes in the
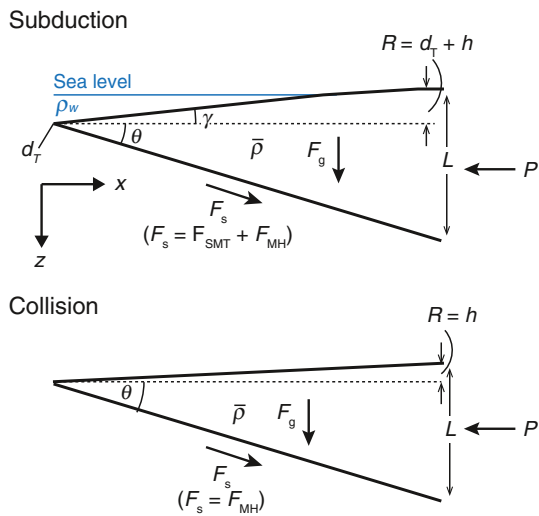
Figure 2. Sketch illustrating the analytical force-balance model for subduction zones and collision zones. $\overline{\rho}$ is the average density of the triangular wedge above the megathrust dipping at angle θ. P is the push of the upper plate, and L is the thickness of the lithosphere above the downdip end of the megathrust. F_g is the gravitational force and F_s is the megathrust shear force. F_{SMT} is the shear force component required to support the submarine margin topography given by trench depth d_T and submarine surface slope γ. F_{MH} is the shear force component required to support subaerial mountain height h. R is the total margin relief. See Section 2 for details.

force balance and the consequences for mountain heights in the upper plate have never been quantified.

Here we evaluate the changes in force balance at the subduction-collision transition based on an analytical force-balance model and finite element models of two plates in frictional contact. In the following, we first outline the conceptual background and introduce the model approaches (Sections 2 and 3). Section 3 also includes a description of the model limitations and a brief comparison to alternative models that have been previously used to investigate the topographic evolution at convergent plate margins. We then present the results of our analysis (Section 4) and afterward discuss our model, also by applying it to active convergent plate margins (Section 5).

2. Conceptual Background

In the presence of margin relief, the gravitational force F_g induces margin-normal deviatoric tension in the upper plate causing a tendency for gravitational collapse (Lamb, 2006; Wang, 1999). This effect of the gravitational force is counteracted by the megathrust shear force F_s, that is, the integrated shear stress along the fault, which causes margin-normal deviatoric compression, thereby providing the lateral support of the upper plate (Figures 1 and 2). If the megathrust shear force exceeds the gravitational effect of margin relief, then the upper plate is under margin-normal deviatoric compression, that is, the horizontal stress σ_x is greater than the vertical stress σ_z. Conversely, if the effect of the gravitational force exceeds the megathrust shear force, then the upper plate is under deviatoric tension and $\sigma_x < \sigma_z$.

Force-balance analysis of convergent plate margins, including ocean-continent subduction zones and continental collision zones, indicates that the effects of the gravitational force and the megathrust shear force are approximately balanced in nature, in which case the stress state underneath the high mountains is near-neutral, that is, $\sigma_x \approx \sigma_z$ (Figure 1a; Dielforder, 2017; Dielforder et al., 2020; Lamb, 2006; Wang & He, 1999; Wang et al, 2019). In detail, the analyses of Lamb (2006) and Dielforder et al. (2020) suggest that σ_x and σ_z are similar within the range of ~10 MPa underneath the high mountains. At this condition, the margin relief is proportional to the megathrust shear force, with a larger relief being associated with greater values of F_s and vice versa. This relation applies equally to subduction and collision zones. However, at ocean-continent subduction zones a substantial part of the margin relief is submarine comprising the elevation difference between the trench and the coast (Figures 1 and 2). Thus, a portion of the megathrust shear force is needed to laterally support the submarine margin topography. Hereafter, we refer to this component of the megathrust shear force as F_{SMT} (Figure 2). The difference between the total shear force F_s and F_{SMT} is the force available to support subaerial mountain height, hereafter referred to as F_{MH}. For collision zones with no submarine margin topography, F_{SMT} is zero and the entire megathrust shear force is available to support subaerial mountain height, that is, F_{MH} equals F_s (Figure 2).

The relation among F_s, F_{SMT}, and F_{MH} is of direct relevance for the force balance around the subduction-collision transition. With the closure of the oceanic basin and progressive underthrusting of continental lithosphere, the submarine margin topography is reduced (Figure 1). Consequently, the gravitational effect of margin relief decreases and so does the shear force component needed to support the submarine margin relief. If the total megathrust shear force F_s remains approximately constant or decreases by an amount less than F_{SMT}, then the reduction of submarine margin relief results in a relative increase of the force available to support subaerial mountain height F_{MH}. If the height of the mountain range remained constant throughout this evolution, then the upper plate would experience enhanced deviatoric compression, because the megathrust shear force would exceed the gravitational effect of margin relief. The finding that mountain heights are at the maximum elevation that is supported by the megathrust shear force indicates, however,

that the increase in deviatoric compression is not sustained in the long-term ($\sim 10^5$–10^6 years). Instead, the increase in compression will facilitate deformation and crustal thickening in the upper plate, which allows the maximum mean elevation (MME) of the mountain range, which is the average height of the main topographic divide, to increase until it reaches the maximum elevation that can be sustained.

3. Methods

3.1. Analytical Force-Balance Model

To evaluate the force balance around the subduction-collision transition, we use a two-dimensional static force-balance model following Dielforder et al. (2020). Our model is based on the analytical expressions of Lamb (2006) and Wang and He (1999), but has been expanded to be applicable to wedges comprising both submarine and subaerial topography, which was not included in the original formulations (for details see Text S1 and Figure S1). The model compares the effects of the gravitational force F_g and the megathrust shear force F_s in the plane of a vertical cross section normal to the plate margin, assuming a triangular wedge overlying the megathrust (Figure 2). If the effects of F_s and F_g are equal and the stress state in the upper plate underneath the high mountains is neutral (that is, $\sigma_x = \sigma_z$), then the force-balance equation for subduction zones can be written as

$$F_s = L\cos\theta\left[\frac{P}{L} - \frac{\overline{\rho}g(L-h)}{2} + \frac{\overline{\rho}gd_T^2}{2L}\left(1 + \frac{(\overline{\rho}-\rho_w)\tan\theta}{\overline{\rho}\tan\gamma}\right)\right], \tag{1a}$$

and for collision zones as

$$F_s = L\cos\theta\left[\frac{P}{L} - \frac{\overline{\rho}g(L-h)}{2}\right], \tag{1b}$$

where θ is the dip angle of the fault, $\overline{\rho}$ is the average density of the wedge, ρ_w is the density of seawater, g is gravitational acceleration, h is mountain height, that is, the maximum mean elevation, and d_T is trench depth. Note that for a neutral stress state underneath the high mountains, the right-hand side of Equation 1a, b represents the effect of the gravitational force resolved parallel to the megathrust. The average density of the wedge is

$$\overline{\rho} = \rho_c\left(1 - \left(\frac{L-z_c}{L}\right)^2\right) + \rho_{mw}\left(\frac{L-z_c}{L}\right)^2, \tag{2}$$

where ρ_c is the average density of the crustal part of the wedge, ρ_{mw} is the average density of the mantle wedge, and z_c is the average thickness of the crust. Parameter P in Equation 1 is the push of the upper plate acting at the back of the wedge. If the stress state underneath the high mountain is neutral, then P can be obtained by integrating the vertical normal stress (Lamb, 2006):

$$P = \int_0^{z=L}\int_0^z \rho(z)g\,dzdz, \tag{3}$$

where z is the depth and ρ is the density. P allows accounting for potential density contrasts between the wedge and the upper plate adjacent to the wedge, for example, due to a partial serpentinization of the mantle wedge. Parameter L is the thickness of the lithospheric wedge above the base of stress transmission, that is, the depth at which the shear stress on the megathrust becomes negligible (Dielforder et al., 2020; Lamb, 2006; Wada & Wang, 2009).

To determine the increase in mountain height required for restoring a balance between the megathrust shear force and the gravitational effect of margin relief after the subduction-collision transition, we can first rewrite Equations 1a and 1b solving for mountain height h

$$h_1 = \frac{2F_{s,1}}{L_1 \bar{\rho}_1 g \cos\theta_1} - \frac{2P_1}{L_1 \bar{\rho}_1 g} - \frac{d_T^2}{L_1}\left(1 + \frac{(\bar{\rho}_1 - \rho_w)\tan\theta_1}{\bar{\rho}_1 \tan\gamma}\right) + L_1, \tag{4a}$$

$$h_2 = \frac{2F_{s,2}}{L_2 \bar{\rho}_2 g \cos\theta_2} - \frac{2P_2}{L_2 \bar{\rho}_2 g} + L_2. \tag{4b}$$

where subscripts 1 and 2 denote the model parameters for the subduction and collision stage, respectively. Subtracting Equation 4a from Equation 4b yields then the required increase in mountain height

$$\Delta h = h_2 - h_1 = \frac{2F_{s,2}}{L_2 \bar{\rho}_2 g \cos\theta_2} - \frac{2F_{s,1}}{L_1 \bar{\rho}_1 g \cos\theta_1} - \frac{2P_2}{L_2 \bar{\rho}_2 g} + \frac{2P_1}{L_1 \bar{\rho}_1 g} + \frac{d_T^2}{L_1}\left(1 + \frac{(\bar{\rho}_1 - \rho_w)\tan\theta_1}{\bar{\rho}_1 \tan\gamma}\right) + L_2 - L_1$$

$$+ \frac{d_T^2}{L_1}\left(1 + \frac{(\bar{\rho}_1 - \rho_w)\tan\theta_1}{\bar{\rho}_1 \tan\gamma}\right) + L_2 - L_1. \tag{5}$$

The increase in upper-plate deviatoric compression that would arise if h did not increase is

$$\Delta\sigma_x = \frac{F_{s,1} - F_{s,2}}{L_2} = \frac{L_1 \cos\theta_1}{L_2}\left[\frac{P_1}{L_1} - \frac{\bar{\rho}_1 g(L_1 - h)}{2} + \frac{\bar{\rho}_1 g d_T^2}{2L_1}\left(1 + \frac{(\bar{\rho}_1 - \rho_w)\tan\theta}{\bar{\rho}_1 \tan\gamma}\right)\right]$$

$$- \cos\theta_2\left[\frac{P_2}{L_2} - \frac{\bar{\rho}_2 g(L_2 - h)}{2}\right]. \tag{6}$$

If the megathrust shear force and other model parameters ($\bar{\rho}$, P, L, and θ) do not change during the subduction-collision transition, then Equations 5 and 6 reduce to

$$\Delta h = \frac{d_T^2}{L}\left(1 + \frac{\Delta\rho\tan\theta}{\bar{\rho}\tan\gamma}\right) = \frac{2F_{SMT}}{L\bar{\rho}g\cos\theta}, \tag{7}$$

$$\Delta\sigma_x = \frac{1}{2L}\bar{\rho}g\cos\theta d_T^2\left(1 + \frac{\Delta\rho\tan\theta}{\bar{\rho}\tan\gamma}\right) = F_{SMT} / L, \tag{8}$$

where F_{SMT} is the shear force component required to support submarine margin topography (see section 2). Note, that F_{SMT} can be obtained by subtracting Equation 1b from Equation 1a

$$F_{SMT} = \frac{1}{2}\bar{\rho}g\cos\theta d_T^2\left(1 + \frac{\Delta\rho\tan\theta}{\bar{\rho}\tan\gamma}\right). \tag{9}$$

3.2. Finite-Element Model

The above analytical expressions provide approximate solutions that describe the basic relation between the margin relief, the megathrust shear force, and the stress underneath the high mountains, but do not provide stress estimates across the wedge overlying the megathrust. To calculate the stresses within the upper plate and to consider isostatic effects, which are not included in the analytical solutions, we use a plane-strain finite-element model of an elastic upper and a rigid lower plate in frictional contact. The basic
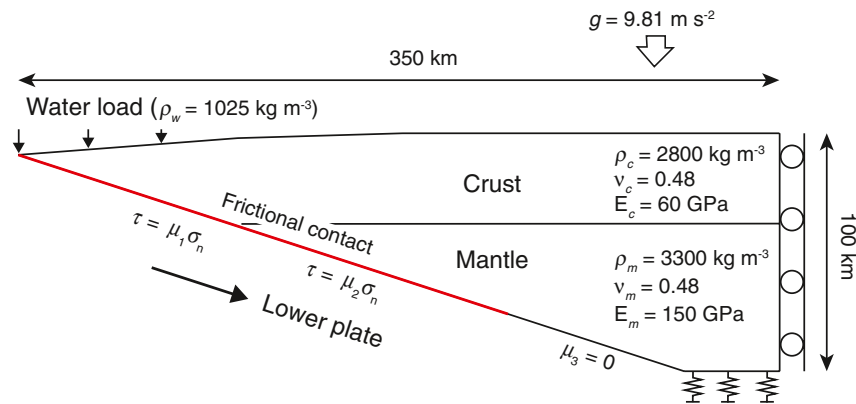
Figure 3. Sketch illustrating the basic setup of the finite-element models with an elastic upper plate and a rigid lower plate. Abbreviations are g acceleration due to gravity, ρ density, ν Poisson ratio and E Young's modulus. Indices c, m and w indicate crust, mantle and water, respectively. The integrated vertical stress P (Equation 3) is part of model results and proportional to the lithostatic stress in the model. The upper part of the plate interface (indicated by red line) is subdivided into two sections with friction coefficients μ_1 and μ_2, while the lower part is frictionless ($\mu_3 = 0$). The values of μ_1 and μ_2 are 0.057 and 0.005 in the subduction stage model, 0.05 and 0.003 in the model representing the stage after trench closure and 0.05 and 0.0024 for the collision stage with increased upper-plate elevation, respectively. The small adjustments in the μ values ensure a constant megathrust shear force for the different models. The right model side may move vertically and the model is isostatically supported by an elastic foundation (indicated by springs) at the base of the upper plate.

model setup, the boundary conditions and rheological parameters are shown in Figure 3. All models were created and calculated using the commercial software ABAQUS (version 6.14) and meshed using linear triangular elements with an average element edge length of ∼1 km. Note that our model setup (Figure 3) follows the modeling approach by Wang and He (1999) and Wang et al. (2019), however, these studies focused on subduction zones and did not present models for the subduction-collision transition. To allow a direct comparison with their subduction-stage models, we also adopted an almost incompressible material ($\nu = 0.48$) for the wedge (Figure 3). Note that using a lower Poisson ratio ($\nu = 0.3$) has an only negligible effect on the results (see Figure S2).

At the beginning of each model run, isostatic equilibrium is established following the procedure described in Hampel et al. (2019). In three different experiments, we then calculated the stress field for a) the subduction stage, b) the stage after trench closure, and c) the collision stage. In the models representing the subduction stage and the stage after trench closure, we assumed an initial elevation of $h = 1.5$ km in the finite-element models, which is reached at 250 km distance from the trench and remains constant further landward to avoid boundary effects from changes in lithospheric thickness near the rear edge of the modeled wedge (cf. Wang & He, 1999). In the model representing the collision stage, the height is $h = 3.25$ km. Note that the solutions of Equations 7 and 8 are actually independent of h.

3.3. Model Limitations and Comparison to Alternative Models

Our force-balance analysis addresses the effect of a change in margin relief at the subduction-collision transition, but does not consider the temporal evolution of the margin topography, convergence rates, or the individual mountain building processes during collision or potential processes leading to plateau formation. The model simplifies the wedge geometry by assuming a planar megathrust and constant surface slope and therefore neglects the local stresses that may result from a more complex surface topography or a curved megathrust. As the force-balance model is two-dimensional, it does not account for affects arising from the three-dimensionality of natural systems. For example, it does not consider the lateral growth of orogens or continental plateaus or the effect of the margin-parallel horizontal stress, which may play a role at margins with oblique plate convergence and strong plate boundary curvature. The above limitations do, however, not affect the general effect of trench closure evaluated in our study. Isostatic effects are not

explicitly included in the analytical formulation but included in the finite-element models. Note that the results from both analytical and numerical models are nevertheless similar with respect to the stress state in the upper plate (see Section 4 below). Finally, we note that our model is applicable to active convergent plate margins comprising a megathrust, but not to old inactive mountain belts, where topographic relief is supported by the strength of rocks rather than the strength of a fault.

Alternative concepts that were used to address topography and mountain height at convergent margins include the classical critical taper theory (Davis et al., 1983; Dahlen, 1990) and mass-balance considerations (e.g., Willett & Brandon, 2002). As the force-balance model, the critical taper theory considers the effects of gravity and the basal shear stress but its solutions are scale-independent and non-unique, that is, a given wedge geometry can be explained by a wide range of strength values as long as the ratio of basal strength to wedge strength remains constant (Davis et al., 1983; Suppe, 2007; Dielforder, 2017). Even more crucial for analyzing the topography at convergent margin is that the critical taper theory assumes a Coulomb plastic rheology, which implies that the shear stress on the basal fault increases unbounded with depth. As a consequence, there is no limit on the maximum possible mountain height. The critical taper model is therefore applicable only to accretionary wedges and fold-and-thrust belts where the basal thrust strength is governed by friction only, but not to the entire upper plate, where viscous deformation is important at deeper levels (Davis et al., 1983; Williams et al., 1994). In comparison, the force-balance models take into account that the shear stress along the plate boundary fault decreases beyond the frictional-viscous transition, which effectively limits the shear force along the fault (Figure 1a) and the mountain height in the upper plate (Lamb, 2006).

In contrast to the critical taper theory and force-balance models, mass-balance considerations assume that mountain belts evolve toward a mass-flux steady state, in which their width and height are related to a balance between the accretionary mass influx and the erosional mass efflux (e.g., Willett & Brandon, 2002). This concept has mainly been used for modeling of eroding critical orogens, and assumes that orogenic wedges grow and shrink in response to changes in the mass fluxes, following arguments of the classical critical taper theory (Roe et al., 2006; Stolar et al, 2006, 2007; Whipple & Meade, 2006). For a critical orogen, the increase in mountain height can therefore be understood as a system response to the new mass flux and would be limited by the achievement of a new mass-flux steady state. Similar to the critical taper theory, however, mass-flux models typically assume a frictional or plastic rheology and do not include the frictional-viscous transition (Roe, 2006; Stolar et al, 2006, 2007; Whipple & Meade, 2006). Furthermore, mass-flux models rely on the scale invariance of the wedge geometry, which allows the model wedge to adjust its size freely. Such a wedge behavior is, however, in conflict with the finite magnitude of forces, which provide the mechanical support of the upper plate (Figure 1), but exhibit no simple dependency on mass fluxes.

4. Analytical and Numerical Results

In this section, we analyze the effects of a reduction of submarine margin topography on the force balance around the subduction-collision transition. First, we consider the end-member scenario in which the megathrust shear force, the dip angle, the thickness of the lithospheric wedge, and the wedge density are identical for the subduction and collision stages (section 4.1). This end-member scenario isolates the effect of submarine margin relief reduction on the force balance and is evaluated based on the analytical model (Equations 7 and 8; Section 4.1.1) and the finite-element models (Section 4.1.2). Subsequently, we evaluate how the results change if we vary the wedge density, megathrust dip angle, or the shear force between the subduction and collision stages (Section 4.2). To ease the presentation of the model results, we refer to a reference model, which is defined by a trench depth of $d_T = 5$ km, a submarine surface slope of $\gamma = 2.9°$, a dip angle of the megathrust of $\theta = 18°$, a thickness of the lithospheric wedge of $L = 75$ km, and an average wedge density of $\bar{\rho} = 2{,}942$ kg m^{-3}, which is equivalent to an upper-plate crustal thickness of 35 km. These parameters were chosen in accordance with the setting at active subduction zones (Amante & Eakins, 2009; Clift & Vannucchi, 2004; Hayes et al., 2018; Wada & Wang, 2009).
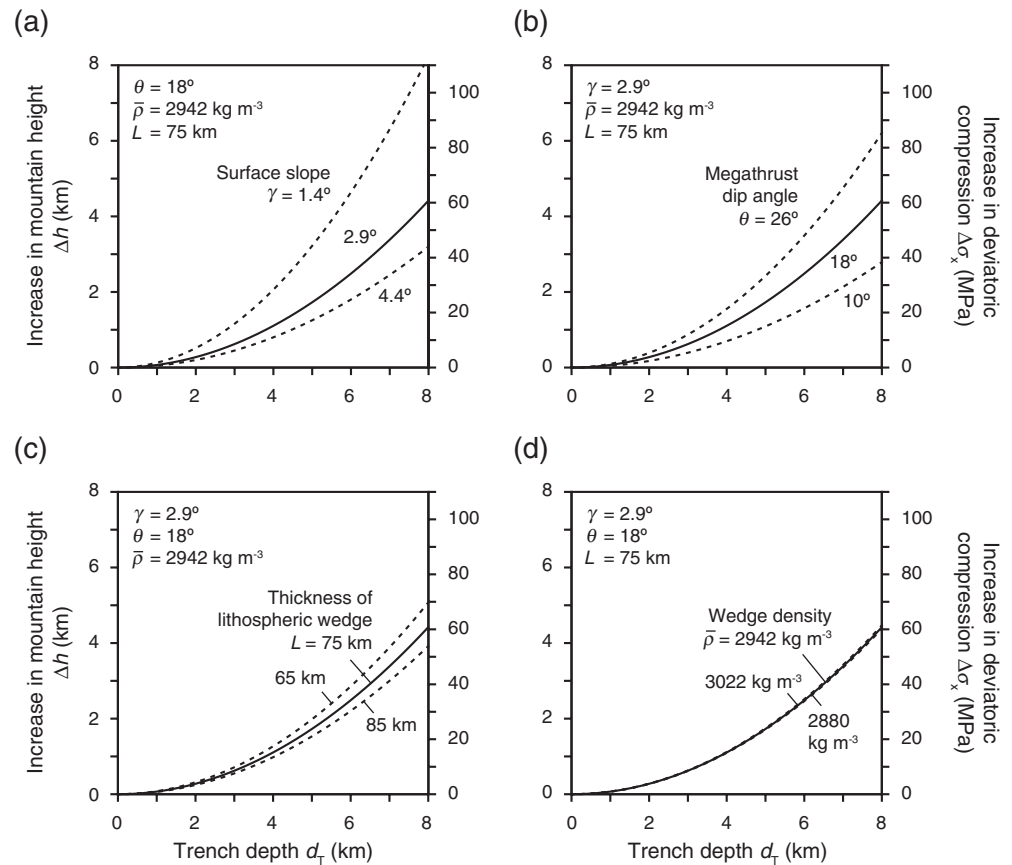
Figure 4. Analytical solutions for the end-member scenario of constant model parameters at the subduction-collision transition. The primary (left) vertical axis shows the increase in mountain height, Δh, required to restore balance between the megathrust shear force and the effect of gravity. The secondary vertical axis indicates the increase in upper plate deviatoric compression, $\Delta\sigma_x$, if mountain height would not increase after the subduction-collision transition. (a–d) Solid lines indicate solutions for the reference model and varying trench depth. Dashed lines indicate solutions for alternative models. All solutions were obtained following Equations 7 and 8. Model parameters as defined in Figure 2.

4.1. End-Member Scenario with Constant Model Parameters

4.1.1. Analytical Results

Figure 4 shows the increase in mountain height Δh required to restore the balance between the megathrust shear force and the effects of gravity during trench closure plotted for different parameters as function of trench depth d_T. In accordance with Equation 7, Δh increases with the square of d_T in all diagrams. For the reference model, the closure of a 5 km deep trench requires an increase in mountain height of $\Delta h \approx 1.73$ km. For comparison, the closure of a 2 km and 8 km deep trench yields $\Delta h \approx 0.28$ km and $\Delta h \approx 4.42$ km, respectively. This relationship varies with the other model parameters. For a given trench depth, a steeper surface slope yields lower values of Δh, while a flatter surface slope yields greater values (Figure 4a). For example, increasing γ by 1.5° decreases Δh by ~28 % relative to the reference model. Conversely, decreasing γ by 1.5° increases Δh by ~87 %. Note, that the changes are not linear because Δh varies with the tangent of γ. The megathrust dip angle has a similar effect on Δh as γ, with the main difference that Δh is directly proportional to the tangent of θ, and thus increases and decreases with increasing and decreasing values of θ, respectively (Figure 4b). For example, increasing or decreasing θ by 8°, increases and decreases Δh relative to the reference model by 40% and 37%, respectively. By comparison, the thickness of the lithospheric wedge or the average wedge density exert a minor control on Δh. Varying L by ±10 km changes the values of Δh by less than 15 % (Figure 4c). Similarly, varying $\overline{\rho}$ in accordance with a change in crustal thickness of ±10 km, affects Δh by only ~1% (Figure 4d).

The increase in upper plate deviatoric compression $\Delta\sigma_x$ that would arise if mountain height remained constant after the subduction-collision transition is shown in Figure 4 for the secondary vertical axis. Because the ratio of $\Delta\sigma_x$ to Δh is constant for the end-member scenario, the curves are identical for the given scale. In accordance with Equations 7 and 8, $\Delta\sigma_x$ shows the same dependency on the model parameters as Δh. For the reference model, $\Delta\sigma_x$ is about 24 MPa. For comparison, the respective values for the closure of a 2 km and 8 km deep trench are $\Delta\sigma_x \approx 4$ MPa and $\Delta\sigma_x \approx 61$ MPa, respectively. Similarly, $\Delta\sigma_x$ varies with the other model parameters, in particular with γ and θ (Figures 4a–4d).

4.1.2. Numerical Results

In this section, we describe the results from the finite-element models representing the subduction and collision stages (Figure 5). Following the above analysis, we report values of (σ_x–σ_z). For comparison, the orientation of the principal stress axes is shown in Figure S3. In all models, the total shear force along the megathrust is about 3.35 TN m^{-1}. In the subduction-stage model, the effects of gravity and F_s are approximately balanced in the upper plate and (σ_x–σ_z) underneath the area of maximum elevation is close to zero in accordance with Equation 1a. The nominal value of (σ_x–σ_z) averaged over the upper 75 km at 250 km distance from the trench is ~1 MPa (see inset in Figure 5a). At this condition, the wedge above the megathrust is under deviatoric compression, with (σ_x–σ_z) being on the order of a few tens of MPa. The greatest compression of about 110 MPa occurs around the downdip end of the upper frictional fault segment at ~35 km depth and is approximately $2\tau_{max}$, where τ_{max} is the maximum shear stress along the megathrust (~55 MPa). With increasing distance to the megathrust, the values of (σ_x–σ_z) decrease, both within the crust and mantle. The offset in(σ_x–σ_z) along the crust-mantle boundary is due to the different densities.

To model the effect of trench closure, we first removed the trench-coast relief, but kept the elevation in the upper plate at 1.5 km (Figure 5b). For this setup, the effects of gravity and F_s are not balanced and the upper plate experiences enhanced deviatoric compression. The average increase in ($\sigma_x - \sigma_z$) at 250 km distance from the wedge tip is $\Delta\sigma_x \approx 22$ MPa, which agrees well with the analytical solution (~24 MPa). The maximum increase in ($\sigma_x - \sigma_z$) occurs at ~90 km distance from the wedge tip and is about 40 MPa. The increased compression in the landward part of the upper plate is also reflected in the orientation of the principal stress axes, which are rotated compared to the subduction stage (Figure S3).

In a second step, we increased the elevation by 1.75 km to $h = 3.25$ km. In accordance with Equation 7, the balance between effects of gravity and F_s is restored with a near-neutral stress state, that is, the average value of (σ_x–σ_z) at 250 km distance is ~0 MPa (Figure 5c). Compared to the subduction zone-reference model in Figure 5a, the wedge above the megathrust experiences slightly stronger deviatoric compression, at least within ~225 km distance from the wedge tip.

4.2. Effects of Changes in Model Parameters Between the Subduction and Collision Stages

As the subduction-collision transition may involve changes in the average wedge density, for example, due to the accretion of sediments and crystalline basement units, as well as in the megathrust dip angle and shear force, we examined how changes of these parameters between the subduction and collision stages affect the force balance solutions. To achieve this, we solved Equations 5 and 6 for the subduction-zone reference model, but assumed different values of $\bar{\rho}$, θ, and F_s for the collision stage. The results are shown in Figure 6 as changes in Δh and $\Delta\sigma_x$ relative to the solutions obtained for the end-member scenario (Figure 4).

A decrease in the average wedge density increases Δh and $\Delta\sigma_x$, because the effect of the gravitational force becomes smaller. However, even for a decrease in $\bar{\rho}$ of about 60 kg m^{-3} (which is equivalent to an increase in crustal thickness of about 10 km), Δh and $\Delta\sigma_x$ increase by ~70 m and ~0.5 MPa, respectively, which is less than 5% relative to the solutions obtained for the end-member model (Figure 6a). Similarly, a steepening or flattening of the megathrust has only a minor effect on Δh and $\Delta\sigma_x$ only. For example, increasing θ by 5° from 18° to 23° increases Δh and $\Delta\sigma_x$ by about 5 % (~100 m and 1 MPa; Figure 6b). In comparison, changing the megathrust shear force has a more pronounced effect on the force-balance solutions. For example, a change of F_s by 1 TN m^{-1}, changes Δh and $\Delta\sigma_x$ by about 60 %, which corresponds to about 1 km and 14 MPa, respectively (Figure 6c).
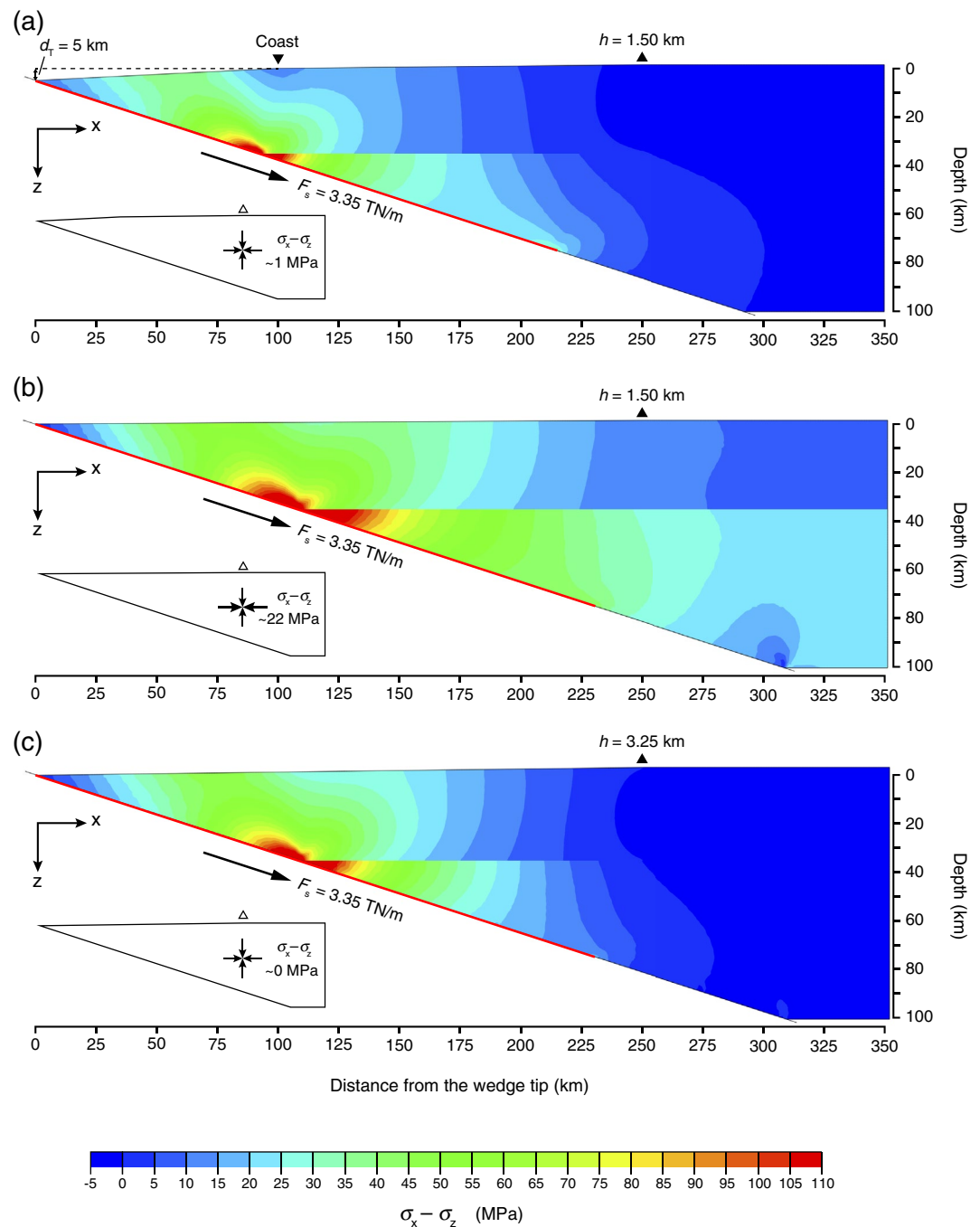
Figure 5. Finite-element models. (a)–(c) The inset in the lower left corner indicates the average value of $(\sigma_x - \sigma_z)$ in the upper 75 km at 250 km distance from the wedge tip. h is mountain height. (a) Subduction zone reference model. d_T is trench depth. (b) Model for the collision stage with mountain height as in (a). Note the increase in the stress $(\sigma_x - \sigma_z)$ in the upper plate, which is caused by the reduction of the submarine margin relief. (c) Model for the collision stage with increased mountain height (3.25 km). The near-neutral stress state in the upper plate is retained by the increase in h.

5. Discussion With Application to Active Convergent Plate Margins

Our analysis indicates that the trench closure at the subduction-collision transition requires an increase in mountain height on the order of several hundred meters to a few kilometers to restore the balance between the effects of gravity and the megathrust shear force. If mountain height did not increase but remained constant, the upper plate would experience enhanced deviatoric compression on the order of tens of MPa.
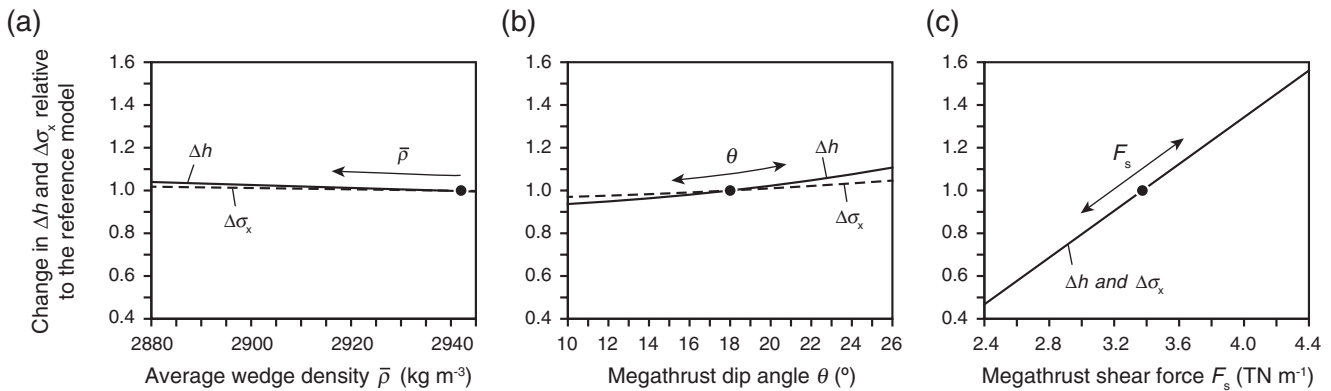
Figure 6. Changes in Δh and $\Delta\sigma_x$ due to a change in model parameters between the subduction stage and the collision stage. (a–c) Parameters as defined in Figure 2. Black dots indicate values as assumed in the reference model (see Section 4.1 and Figure 4).

This stress increase would ultimately facilitate tectonic shortening, thickening and hence an increase in mountain height. Only if the megathrust shear force decreased by the same (or larger) amount as the effect of the gravitational force, an increase in elevation would not be supported. In this case, the mountain height would remain constant or even decrease, whereas the upper plate would experience extension, which is at odds with geological constraints on incipient continental collision (see Sections 1 and 5.3).

The analytical solutions presented in this study are consistent with the finite element models and provide an easy means to assess the principal effect of trench closure on the force balance at the subduction-collision transition. In addition, the finite-element models provide details on upper-plate stresses that cannot be assessed from the analytical solutions, for example, the numerical models show the magnitude of the stress field throughout the upper plate (Figure 5). Note that the purely elastic finite-element models are designed to illustrate the stress field but do not capture the actual permanent deformation during collision. The solutions shown in Figures 4 and 5 were obtained for the end-member scenario of constant model parameters (wedge density, megathrust dip angle, thickness of the lithosphere, and megathrust shear force). The variation of the model parameters (Section 4.2) indicates that especially a change in the megathrust shear force may alter the expected increase in mountain height during collision (Figure 6). To further explore the influence of the megathrust shear force, the following Section 5.1 discusses the main factors that control the magnitude of the shear force and provides estimates of F_s for collision zones. Afterward, we apply our force-balance models to the Arabian Eurasian convergent plate boundary, which exhibits a lateral transition from subduction to collision, and to other active natural subduction zones to evaluate the increase in mountain height if these margins transitioned into collision zones (section 5.2).

5.1. Constraints on the Magnitude of the Megathrust Shear Force

As shown in Figure 6, changes in wedge density or megathrust dip angle have little impact on the force-balance solutions but a change in the megathrust shear force can considerably affect the increase in mountain height that is required to restore a balance between the effects of gravity and F_s. Such a change in the megathrust shear force during the subduction-collision transition may be caused, for example, by a slowdown in plate convergence rates, because such a deceleration may decrease the strain rate along the plate boundary and hence the shear stress on the viscous fault segment (e.g., van den Beukel, 1992).

Although the shear force changes at the subduction-collision transition are difficult to assess in detail, the following considerations may help to shed some light on the magnitude of the shear force and its potential changes after the onset of collision. In principle, the magnitude of F_s depends mainly on the effective frictional strength of the fault (μ') and the depth of the frictional-viscous transition (z_{FVT}), where F_s increases with both parameters (Lamb, 2006; van den Beukel, 1992; Wang & He, 1999). Independent constraints on the effective strength of collision megathrusts obtained for the Himalayas, Taiwan, and the European Alps indicate μ' values of about 0.05–0.1 (Carena et al., 2002; Dal Zilio et al., 2019; Dielforder, 2017;

Suppe, 2007). These values are slightly higher than the typical μ' value of about 0.03 inferred for many subduction megathrusts, but still overlap with the total range of μ' values of 0.02–0.13 that have been inferred from heat-dissipation models and force-balance models for subduction megathrusts around the globe (X. Gao & Wang, 2014; Lamb, 2006; Seno, 2009). This suggests that the frictional strength of collision and subduction megathrusts is comparable within a factor of ~5.

The depth of the frictional-viscous transition (FVT) at collision zones is most likely controlled by the onset of crystal-plastic deformation in quartz-rich lithologies at temperatures above 300°C–350°C (Davis et al., 1983; Stipp et al., 2002; van den Beukel, 1992). For an average interseismic or bulk geological strain rate of about $10^{-14 \pm 1}$ s^{-1}, a thermal gradient between 15°C and 25°C km^{-1}, and dislocation creep in quartz, this suggests that the FVT occurs at 15–25 km depth (Davis et al., 1983; Fagereng & Biggs, 2019; Hirth et al., 2001). This estimate is consistent with inferences about the FVT for the Himalayas, the Zagros, the European Alps, and the Variscides, and agrees with geodetically constrained locking depths of continental fault zones (Ader et al., 2012; Dielforder et al., 2016; Fagereng & Biggs, 2019; Oncken et al., 1999; Tavani et al., 2018; Wright et al., 2013). Another factor that affects the magnitude of F_s is the base of stress transmission, that is, the depth at which the shear stress on the fault becomes negligible (z_{base}). At subduction zones, this depth lies at about 70–80 km depth, but it may be shallower at collision zones due to a higher thermal gradient (Dielforder et al., 2020; Lamb, 2006; Wada & Wang, 2009).

From the constraints given above, the approximate range of the megathrust shear force that can be expected for collision zones can be estimated following Dielforder et al. (2020). As illustrated in the inset diagram in Figure 1a, the magnitude of the shear force can be computed as the area beneath the curve representing the shear stress along the along the plate boundary fault. Using values for the base of stress transmission of 75 km and 65 km depth and values between 10 and 30° for the megathrust dip angle, we varied the effective frictional strength μ' and the depth of the frictional-viscous transition z_{FVT} between 0.05-0.1 and 15–25 km, respectively. Figure 7a shows the diagram for z_{base} = 75 km. For a FVT at 25 km depth, the shear force per unit length varies between ~1.6 and 8.3 TN m^{-1}, with an average value of about 3.7 TN m^{-1}. For a shallower FVT at 15 km depth, F_s varies between ~0.9 and ~4.8 TN m^{-1}, with an average value of about 2.1 TN m^{-1}. In other words, F_s is about 40 % lower for the shallower FVT. For comparison, decreasing the base of stress transmission to z_{base} = 65 km, decreases F_s on average by about 0.6 TN m^{-1} or 20 % (Figure 7b). Taken together, the above estimates suggest that the megathrust shear force per unit length should be on the order of a few TN m^{-1} at collision zones. The mean value and one standard deviation of all solutions is about 2.6 ± 1.4 TN m^{-1}.

5.2. Application to Active Convergent Plate Margins

5.2.1. Arabian-Eurasian Convergent Plate Boundary

The Arabian-Eurasian convergent plate boundary exhibits a lateral transition from subduction in the east to continental collision in the west, which allows us to compare differences in the margin relief across the transition with solutions of the force-balance model obtained from our end-member scenario (Figures 8 and 9, Tables 1 and 2). In the east at the Makran subduction zone, oceanic lithosphere subducts northward at a low angle of about 10° ± 2° beneath Eurasia (Byrne et al., 1992; DeMets et al., 2010; Hayes et al., 2018; Penney et al., 2017; Vernant et al., 2004). A characteristic of the Makran subduction zone is the large accretionary complex that extends onshore and offshore and is built by the thick sedimentary cover of the incoming oceanic plate (Burg, 2018; Fruehn et al., 1997; J. P. Platt et al., 1985). The thick sediments condition a shallow trench depth of about 3–3.5 km and a gentle submarine surface slope of about 1.3°–1.7° (Figure 9).

Around the Strait of Hormuz, the Makran subduction zone transitions into the Zagros collision zone that formed in response to continental collision between Arabia (lower plate) and Eurasia (upper plate). The exact timing of onset of collision remains controversial, but most studies agree that collision was underway by the end of the Oligocene (Barber et al., 2018; Koshnaw et al., 2018; McQuarrie & van Hinsbergen, 2013; Mohammad & Karim, 2019; Mouthereau et al., 2012). A prominent tectonic feature of the Zagros collision zone is the large, southward-propagating foreland fold and thrust belt that develops on the Arabian plate
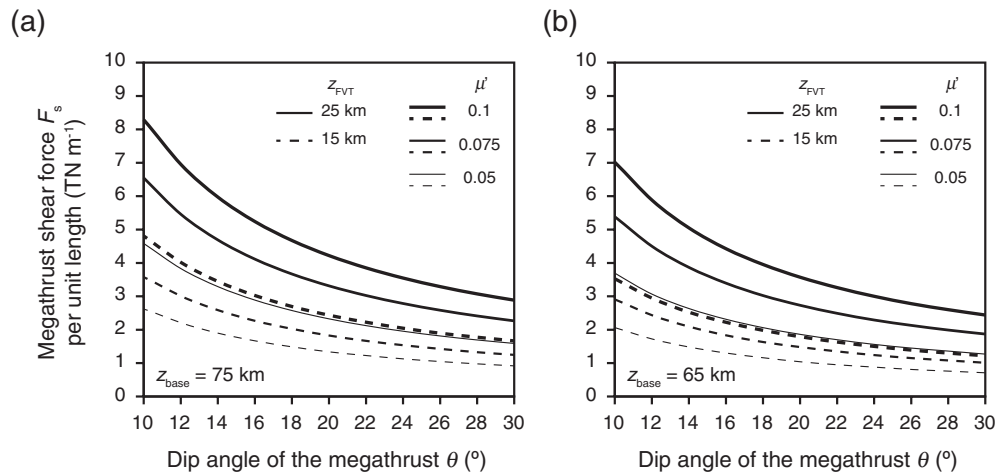
Figure 7. Estimates of the megathrust shear force F_s for collision zones. The solutions shown in (a) and (b) were calculated for a base of stress transmission, z_{base}, at 75 km and 65 km depth, respectively. Parameter μ' is the effective frictional strength of the megathrust, z_{VFT} is the depth of the frictional-viscous transition. All values of F_s were calculated following Dielforder et al. (2020).

(Alavi, 1994; Molinaro et al., 2005; Vergés et al., 2011). In the Fars area, the present-day deformation front lies up to 350 km south of the actual suture zone, the Main Zagros Thrust (MZT). The basal detachment of the fold and thrust belt is located at or close the basement-cover contact within weak lithologies (evaporites, shales) and connects at depth to basement faults that may root in the MZT (Garzic et al., 2019; Molinaro et al., 2005; Tavani et al., 2018; Vergés et al., 2011). The detailed geometry of the principal plate boundary fault remains, however, unknown.

The lateral subduction-collision transition is accompanied by a prominent change in margin topography (Figure 9). The submarine margin relief off the Makran margin decreases almost entirely toward the west while mountain height in the upper plate increases. To quantify the differences in elevation, we determined the maximum mean elevation along 100-km-wide swath profiles running across the Makran subduction zone and Zagros collision zone. Two swath profiles are shown in Figure 9b as an example. Overall, the MME
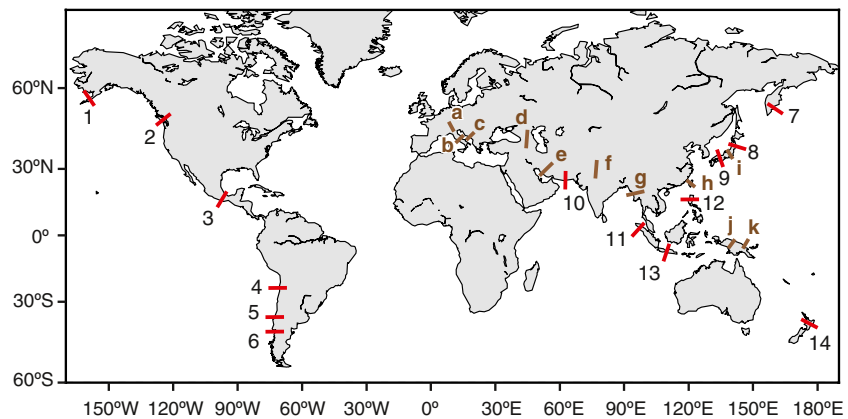

Figure 8. World map showing the localities of subduction zone transects (1–14) and collision zones (a)–(k) considered in the force-balance analysis and used for the evaluation of collisional mountain heights, respectively. Subduction zones: 1, West Alaska; 2, Northern Cascadia; 3, Mexico; 4, 5, and 6, Andes at 23°S, 36°S, and 41°S, respectively; 7, Kamchatka; 8, Japan Trench; 9, Nankai Trough; 10, Makran; 11, Northern Sumatra; 12, Manila; 13, Java; 14, Northern Hikurangi. Collision Zones: a, European Alps; b, Apennines; c, Dinaric Alps; d, Greater Caucasus; e, Zagros; f, Himalayas; g, Indo-Burma ranges; h, Central Taiwan orogen; i, Izu-Bonin arc collision; j, Papuan fold belt; k, Finisterre. The Map was created using the Python package Matplotlib (Hunter, 2007).

Table 1
Input parameters Force-Balance Analysis

No	Margin	d_T (km)[a]	MME (km)[b]	R (km)[c]	γ (°)[d]	θ (°)[e]	z_c (km)[f]
1	West Alaska	5.3	0.8 ± 0.5	6.1 ± 0.6	4.0	13	30
2	Northern Cascasdia	2.5	1.8 ± 0.5	4.3 ± 0.5	1.4	14	35
3	Mexico	5.2	2.9 ± 0.3	8.1 ± 0.4	4.9	14	40
4	Andes, 23°S	7.6	4.7 ± 0.3	12.3 ± 0.3	5.4	19	60
5	Andes, 36°S	5.0	2.6 ± 0.6	7.6 ± 0.6	3.0	18	40
6	Andes, 41°S	4.3	1.3 ± 0.4	5.6 ± 0.5	2.3	19	35
7	Kamchatka	7.6	1.1 ± 0.3	8.7 ± 0.3	2.2	19	35
8	Japan Trench	7.6	0.8 ± 0.3	8.4 ± 0.4	2.0	15	30
9	Nankai Trough	4.5	0.6 ± 0.5	5.1 ± 0.5	2.2	16	30
10	Central Makran	3.3	1.5 ± 0.3	4.8 ± 0.4	1.5	10	40
11	Northern Sumatra	4.9	1.6 ± 0.4	6.5 ± 0.5	2.2	15	30
12	Manila	4.2	0.9 ± 0.5	5.1 ± 0.5	1.8	22	40
13	Java	7.0	1.1 ± 0.6	8.1 ± 0.6	1.6	17	35
14	Northern Hikurangi	3.1	1.0 ± 0.2	4.1 ± 0.3	1.2	15	30

[a]Uncertainty on the trench depth (d_T) is taken to be ±0.2 km. [b]Maximum mean elevtion (MME). Given uncertainties are 1 s.d. [c]Margin relief (R). Given uncertainties are the propagated uncertainties on d_T and MME. [d]Uncertainty on the submarine surface slope (γ) is taken to be ±0.2°. [e]Uncertainty on the average megathrust dip angle (θ) is taken to be ±2°. [f]Crustal thickness (z_c) used to calculate the average wedge density. Uncertainty is taken to be ±5 km.

Table 2
Results of the Force-Balance Analysis

No.	Margin	F_s[a,b](TN m^{-1})	F_{SMT}[a,c](TN m^{-1})	F_{MH}[a,d](TN m^{-1})	Δh[a,e](km)	$\Delta\sigma_x$[a,f](MPa)	H-MME[g] (km)
1	West Alaska	2.61 ± 0.54	1.26 ± 0.1	1.35 ± 0.54	1.2 ± 0.1	16.8 ± 1.4	2.0 ± 0.5
2	Northern Cascasdia	2.91 ± 0.47	0.67 ± 0.09	2.24 ± 0.46	0.5 ± 0.1	8.9 ± 1.3	2.2 ± 0.5
3	Mexico	4.38 ± 0.37	1.08 ± 0.08	3.30 ± 0.37	1.1 ± 0.1	14.4 ± 1.1	4.0 ± 3.3
4	Andes, 23°S	7.42 ± 0.31	2.73 ± 0.15	4.69 ± 0.27	2.8 ± 0.2	36.4 ± 2.4	7.5 ± 0.3
5	Andes, 36°S	4.59 ± 0.48	1.70 ± 0.13	2.89 ± 0.46	1.7 ± 0.2	22.6 ± 1.9	4.2 ± 0.6
6	Andes, 41°S	3.30 ± 0.44	1.66 ± 0.11	1.65 ± 0.42	1.6 ± 0.2	22.1 ± 2.0	2.9 ± 0.4
7	Kamchatka	6.86 ± 0.54	5.37 ± 0.40	1.50 ± 0.37	5.3 ± 0.5	71.6 ± 5.9	6.4 ± 0.3
8	Japan Trench	6.18 ± 0.62	4.89 ± 0.42	1.29 ± 0.47	4.7 ± 0.5	65.3 ± 6.0	5.4 ± 0.3
9	Nankai Trough	2.77 ± 0.52	1.67 ± 0.15	1.10 ± 0.50	1.6 ± 0.2	22.3 ± 2.2	2.2 ± 0.5
10	Central Makran	2.66 ± 0.35	0.82 ± 0.11	1.84 ± 0.33	0.8 ± 0.1	11.0 ± 1.5	2.3 ± 0.3
11	Northern Sumatra	4.05 ± 0.52	1.88 ± 0.17	2.17 ± 0.50	1.8 ± 0.2	25.1 ± 2.4	3.4 ± 0.4
12	Manila	3.31 ± 0.42	2.17 ± 0.2	1.14 ± 0.37	2.2 ± 0.2	29.0 ± 2.9	3.1 ± 0.5
13	Java	6.96 ± 0.70	5.49 ± 0.51	1.47 ± 0.48	5.3 ± 0.6	73.2 ± 7.3	6.4 ± 0.6
14	Northern Hikurangi	2.82 ± 0.47	1.28 ± 0.17	1.55 ± 0.44	1.2 ± 0.2	17.0 ± 2.4	2.2 ± 0.2

[a]Given uncertainty represent the 1 standard deviation of 100.000 model solutions, in each of which the model parameters were randomly varied within the range of uncertainties (Table 1). Calculations following Dielforder et al. (2020). [b]Megathrust shear force (F_s); calculated from Equation 1a. [c]Shear force required to support the submarine margin topography (F_{SMT}); calculated from Equation 9. [d]F_{MH} is the component of F_s available to support subaerial mountain height; $F_{MH} = F_s - F_{SMT}$. [e]Increase in mountain height required to retain force equilibrium (Δh); calculated from Equation 7. [f]Increase in upper plate compression, if mountain height does not increase ($\Delta\sigma_x$); calculated from Equation 8. [g]Hypothetical maximum mean elevation (H-MME) for the collision stage at force equilibrium. Given uncertainties are the propagated uncertainties on the MME (Table 1) and Δh.
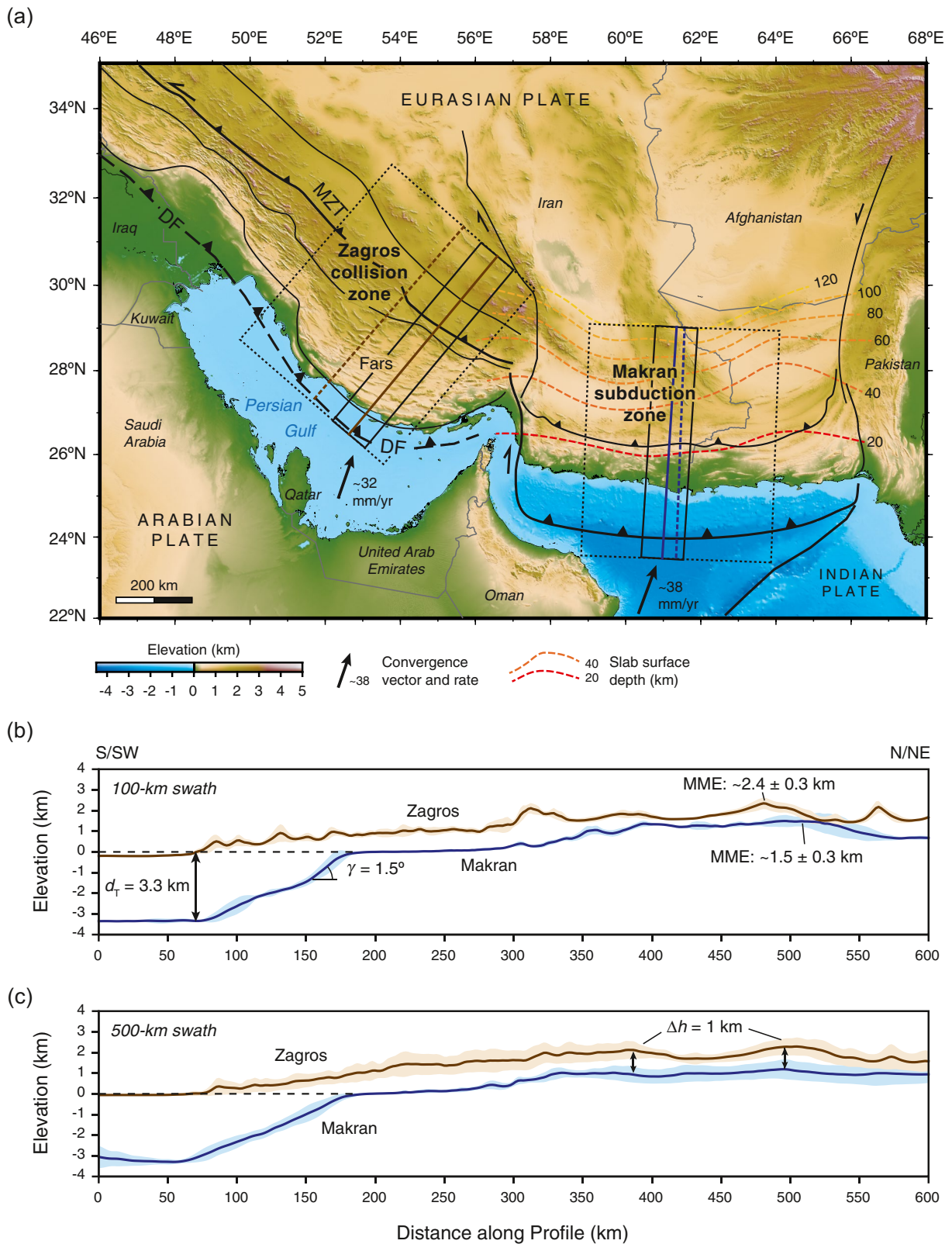
Figure 9.

varies between 1.4 and 1.8 km for Makran and between 2.3 km and 3.0 km for Zagros, suggesting an average elevation difference of about 1 km across the subduction-collision transition. For comparison, we also show two 500-km-wide swath profiles across the Makran and Zagros, which also indicate a difference in average mountain height of about 1 km (Figure 9c).

This change in mean elevation agrees well with our force-balance solution, which yield an increase in mountain height of 0.8 km for the Makran subduction zone (Table 2). In other words, the present-day mountain height at the Zagros collision zone is consistent with a pre-collisional margin topography comparable to the present-day relief at the Makran (e.g., François et al., 2014). Moreover, it implies that the shear force per unit length on the megathrusts beneath the Makran subduction zone and Zagros collision zone must be approximately equal at present and about 2.7 ± 0.5 TN m^{-1}. This value of F_s agrees well with the above constraints on the megathrust shear force (Section 5.1) and would be consistent with a shallow dipping fault and with an effective frictional strength of about 0.05, given that FVT is at about 20–25 km depth at the Zagros collision zone (Tavani et al., 2018). For comparison, the frictional strength of the Makran subduction megathrust has been previously constrained to ∼0.03 (Penney et al., 2017; Smith et al., 2013).

5.2.2. Hypothetical Collisional Mountain Heights for Active Subduction Zones

In this section, we apply our force-balance model to other active subduction zones to determine the hypothetical MMEs that would result if these margins transitioned into collision. To achieve this, we first solved the force balance for these margins for the current subduction stage following Equation 1 (Tables 1 and 2). Figure 10a shows the solutions for the megathrust shear force per unit length plotted against the present-day margin relief R. Overall, R increases with F_s, from about 4 km and <3 TN m^{-1} to about 12 km and 7 TN m^{-1}. The mean value and one standard deviation of all solutions of F_s is about 4.3 ± 1.8 TN m^{-1}. The apparent scatter in Figure 10a results from differences in the submarine margin topography and the megathrust dip angle (Table 1). For comparison, Figure 10b shows the MMEs plotted against F_s. In total, the MMEs vary between 0.6 km and 4.7 km, although most MMEs are less than 2 km. Note that there is no simple relation between the MME and F_s, because for subduction zones the MME correlates only with the shear force component F_{MH} (section 2; Dielforder et al., 2020). In a second step, we evaluated the increase in MME required to restore the balance between F_s and the effect of gravity (Figures 10c and 10d). Overall, Δh varies between 0.5 and 5.3 km, with most values being 2.5 km or less. Adding Δh to the present-day MMEs yields the hypothetical elevations for the collision stage. These MME values vary between 2 km and 7.5 km (Figures 10e and 10f).

Compared to the modern collision zones, we find that the majority of our calculated hypothetical MMEs falls into the range of present-day mountain heights, which show MMEs between 1.4 and 5.5 km (Table 3, Figures 10e and 10f). Only the hypothetical MMEs for the central Andes at 23°, Kamchatka, the Japan Trench, and Java (4, 7, 8, and 13 in Figures 8 and 9) plot around or above 5.5 km. These MMEs were obtained for margins, at which the shear force per unit length exceeds 6 TN m^{-1}. This relation reflects that the MME increases by about 1 km per TN m^{-1} (Figure 10e; Dielforder et al., 2020). Furthermore, all these margins are associated with a deep trench ($d_T \geq 7$ km). For Kamchatka, Japan, and Java the deep trench coincides with a low submarine surface slope γ, or a great distance between the trench and the coast, which causes a great gravitational effect of the submarine margin topography and large shear force component F_{SMT} (Tables 1 and 2). Accordingly, the increase in mountain height required to restore the force balance is exceptionally large, which leads to the high hypothetical MMEs, despite present-day mountain heights of about 1 km or less. By comparison, the trench-coast distance is shorter for the central Andes, which translates to a moderate increase in mountain height of about 2.8 km. As the central Andes are already the second highest mountain belt on Earth, such an increase in mountain height results in an exceptionally high hypothetical MME.

Figure 9. Arabian-Eurasian convergent plate boundary. (a) Tectonic overview map based on Burg (2018), Penney et al. (2017), and Vergés et al. (2011). Background SRTM15+ digital elevation model from Tozer et al. (2019). Slab surface depths from Hayes et al. (2018). Plate convergence rates and vectors from DeMets et al. (2010). Solid blue and brown lines and associated rectangles indicate the 100-km-wide swath profiles shown in (b). Dashed lines and rectangles indicate the 500-km-wide swath profiles shown in (c). (b) and (c) 100-km-wide and 500-km-wide swath profiles across Makran (blue) and Zagros (brown). The blue and brown lines indicate the mean elevation. Shaded area is the 1 standard deviation on the mean elevation. Swath profiles calculated from the ETOPO1 digital elevation model (Amante & Eakins, 2009) using TopoToolbox for MATLAB (Schwanghart & Scherler, 2014).
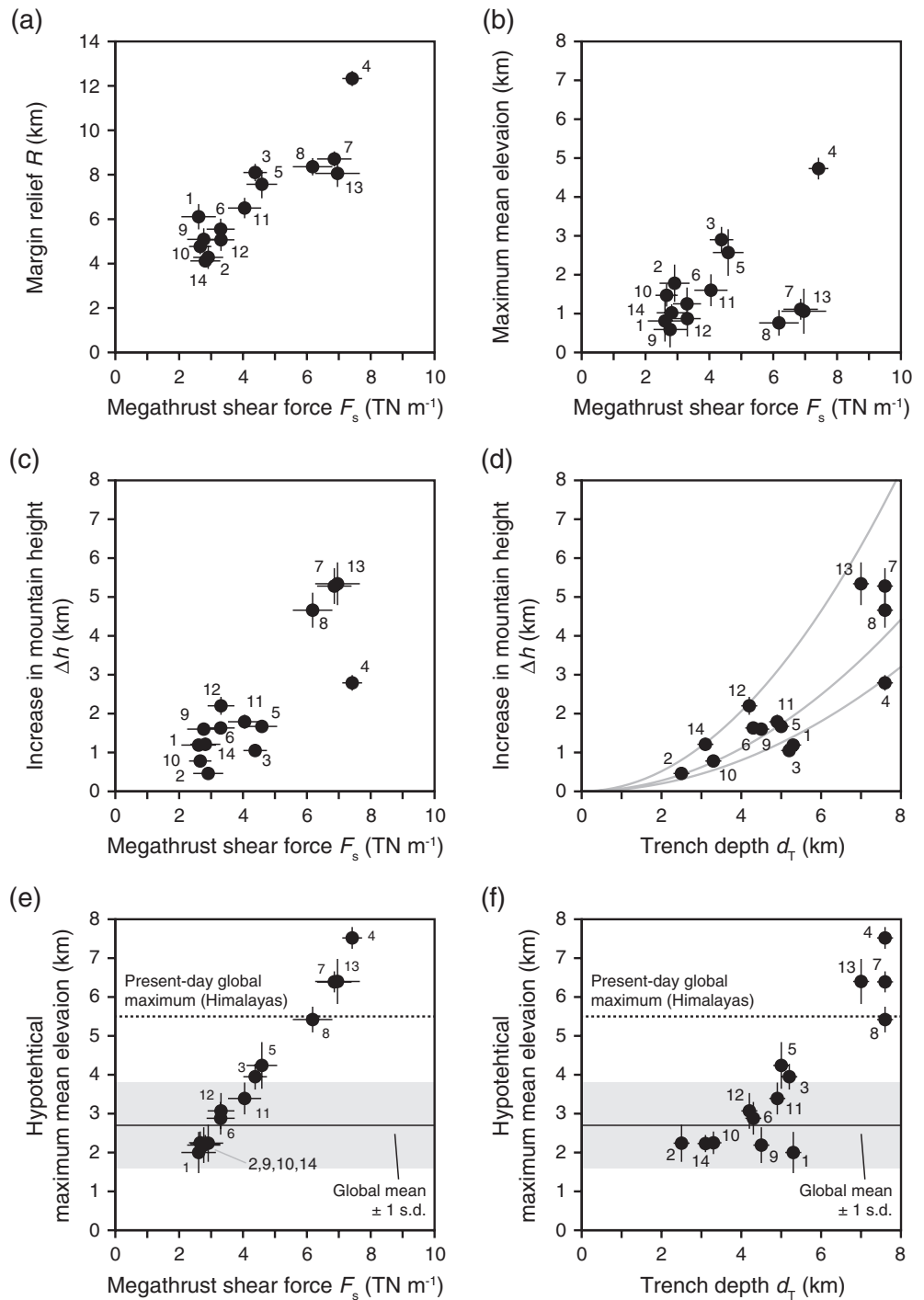
Figure 10. Prediction of the force-balance analysis on the expected elevation changes for present-day subduction zones during future subduction-collision transitions. (a–f) Numbering as in Figure 8 and Tables 1 and 2. Error bars are the 1 standard deviation resulting from the uncertainties on model parameters as given in Table 1. (d) Gray curves indicate the solutions shown in Figure 4a for reference. (e) and (f) black dashed lines at 5.5 km elevation indicate the approximate present day maximum mean elevation (MME) of the Himalayas. The solid black line and gray rectangle indicate the mean value and one standard deviation, respectively, of the MME of global collision zones (Figure 8, Table 3).

Table 3
Maximum Mean Elevation at Collision Zones

ID[a]	Collision zone	MME[b] (km)
a	European Alps	2.49 ± 0.56
b	Apennines	1.40 ± 0.16
c	Dinaric Alps	1.55 ± 0.25
d	Greater Caucasus	2.90 ± 0.63
e	Zagros	2.70 ± 0.42
f	Himalayas	5.46 ± 0.27
g	Indo-Burma ranges	1.90 ± 0.38
h	Central Taiwan orogen	2.63 ± 0.47
i	Izu-Bonin collision	1.76 ± 0.51
j	Papuan fold belt	3.39 ± 0.44
k	Finisterre range	3.05 ± 0.31

[a]ID as in Figure 8. [b]Maximum mean elevation (MME) and 1 s.d as obtained from 100-km-wide swath profiles.

Although it cannot be ruled out that mountain belts in future geological times may reach such high MMEs, we argue that this may be unlikely for the following reasons. For the subduction zones of Japan, Java, Kamchatka, and the central Andes, the values of F_s exceeding 6 TN m^{-1} relate to a very deep FVT at about 50–60 km depth. This depth of the FVT has been constrained from earthquake depth distributions and the lowermost occurrence of reverse faulting events on the megathrust, which mark the approximate downdip limit of the frictional fault segment (e.g., X. Gao & Wang, 2014; Hayes et al., 2012; Heuret et al., 2011, Sippl et al., 2018). In contrast, our above analysis (Section 5.1) suggests that at collision zones, where the FVT transition is much shallower, values of F_s exceeding 6 TN m^{-1} require a combination of a shallowly dipping (<14°) and rather strong fault ($\mu' \approx 0.1$). Although such conditions may be almost matched at the Himalayan collision zone, where F_s is about 5 ± 1 TN m^{-1} (Dielforder et al., 2020), they seem rather uncommon. We therefore argue that for subduction zones settings, for which F_s exceeds ~6 TN m^{-1}, the megathrust shear force tends to decrease at the subduction-collision transition, mainly because the FVT will rise to shallower levels. A decrease in the megathrust shear force is also suggested by the difference of 1.7 TN m^{-1} in the mean values of F_s obtained for active subduction zones from Equation 1 (4.3 ± 1.8 TN m^{-1}) and for collision zones from our estimates based on the computation of the shear force magnitude (2.6 ± 1.4 TN m^{-1}, Section 5.1).

5.3. Implications for Mountain Building

As outlined in the previous section, the average magnitude of F_s at collision zones is similar to or even smaller than the one at subduction zones. This indicates that the increase in mountain height at the subduction-collision transition does not require an increase in F_s, but is already supported by the reduction of submarine margin topography. In contrast, mountain building and enhanced upper-plate compression at oceanic subduction zones has been associated with an increase in the shear force (Lamb & Davis, 2003; Luo & Liu, 2009). In case of the Andean margin, the shear force increase and the resulting rise of the central Andes were likely induced by a reduced sediment input to the trench (Lamb & Davis, 2003), although mountain building may have been triggered by additional processes such as slab anchoring (e.g., Faccenna et al., 2017). As noted by Lamb and Davis (2003), the shear force increase may also explain the observed deceleration of the relative plate convergence between the Nazca and South American Plates (Norabuena et al., 1999; Seton et al., 2012).

While our study constrains the increase in mountain height required to restore the balance between the megathrust shear force and the effect of gravity, it does not determine how mountain height evolves with respect to temporal changes in the force balance. The subduction of a passive margin typically requires some million years, depending on its width and the plate convergence rate (e.g., Barber et al., 2018; Ford et al., 2006; Kapp & DeCelles, 2019; McIntosh, et al., 2013). During this process, the submarine relief reduction will increase the deviatoric compression in the upper plate, but the intensity of compression will depend on how mountain height evolves with respect to changes in the force balance. The height increase may occur on timescales of 10^6–10^7 years, as indicated by the data from the European Alps (Campani et al., 2012; Schlunegger & Kissling, 2015), the Himalayas (Ding et al., 2017; Gébelin et al., 2013; Xu et al., 2018), and Papua New Guinea (Abbott et al., 1997; Cloos et al., 2005). One scenario is that the increase in mountain height keeps pace with the decrease in margin relief in a way that an approximate balance between the effects of gravity and megathrust shear force is continuously maintained. This scenario would imply that the deviatoric compression does not increase substantially and requires that the tectonic processes around the subduction-collision transition just cause the appropriate increase in elevation. Another scenario is that the increase in elevation lags behind the changes in the force balance, in which case the deviatoric compression of the upper plate increases, at maximum by $\Delta\sigma_x$. We consider this second scenario more plausible, because

the implied transient imbalance between the effects of F_s and gravity is more consistent with geological observations on wedge-internal deformation during incipient continental collision, involving, for example, out-of-sequence thrusting, back-thrusting, and (re)folding of accreted basement units (e.g. Dielforder et al., 2016; Maxelon & Mancktelow, 2005; Scheiber et al., 2012; Tate et al., 2015; Vergés et al., 2011; Wiederkehr et al., 2008). The deformation in the wedge will contribute to an increase in mountain height. For example, large out-of-sequence thrusts, that splay from the plate boundary and cut through the orogenic wedge, can cause substantial thickening within the thrust wedge. An example for this is the basal thrust system of the Helvetic nappes in the European Alps that was active as out-of-sequence thrust and caused km-scale thickening (Pfiffner, 1986). Perhaps even more important for the increase in mountain height is crustal thickening due to accretionary processes, in particular the basal accretion of crystalline basement units, which adds mass to the orogenic wedge (R. Gao et al., 2016; McIntosh et al., 2013; Oncken et al., 1999; Rosenberg & Berger, 2009; Scheiber et al., 2012). The accretionary mass influx depends on the convergence rate and the size of the accreted units, and may thus be a limiting factor. In addition, the mass influx is counteracted by erosion, which may accelerate with increasing elevation and hence retard the increase in mountain height (e.g., Montgomery & Brandon, 2002; Whipple & Meade, 2006).

The above considerations hint at another closely related aspect of the subduction-collision transition, that is, the temporal relation between the arrival of the passive continental margin at the trench and the onset of orogenesis. Previous studies have argued for a possible delayed onset of orogenesis and a protracted phase of continental subduction preceding continental collision (e.g., Barber et al., 2018; Regard et al., 2003). The phase of continental subduction is thought to relate to the underthrusting of the rifted and possibly hyperextended continental margin, which is favored by the limited buoyancy of thinned continental crust (Cloos, 1993; Ranalli et al., 2000). During this stage of continental subduction, the foreland basin is typically underfilled and remains marine (e.g., Sinclair & Allen, 1992), which suggests that the decrease in submarine margin relief is rather small. In this case, an approximate balance between the effects of gravity and F_s may be maintained without major elevation changes. However, with the underthrusting of thicker continental crust the foreland basin becomes eventually filled and the submarine margin relief decreases (Figure 1b). At this stage, mountain height must increase by Δh and, if the gain in elevation lags behind, the deviatoric compression increases, which facilitates upper-plate tectonic shortening. Our findings are thus consistent with the inference that mountain building may initiate well after the arrival of the passive continental margin at the trench and suggest that the evolution of the margin relief has a great impact on this.

Another aspect of continental collision is the slowdown in plate convergence rates, which reflects an increase in resistive forces (e.g., McKenzie, 1969). These forces include the megathrust shear force and the positive buoyancy of continental crust, which both act on the subducting slab and might change during the subduction-collision transition (Cloos, 1993; van den Beukel, 1992). The slowing of plate convergence has been further attributed to the development of high mountain topography (Copley et al., 2010; Molnar & Stock, 2009). For example, Copley et al. (2010) showed that the slowdown in the rate of India-Eurasia convergence around the estimated time of collision, and the change in the position of the India-Eurasia Euler pole, are consistent with an increase in the horizontal force acting on the Indian plate. According to Copley et al. (2010), this correlation reflects an increase in the gravitational potential energy due to mountain building in the Himalaya-Tibet area, which increased the resistance to plate convergence. However, this interpretation did not consider the gravitational effect of the Eurasian continental margin in the region of Tibet during the subduction of Paleo-Tethys preceding the Himalayan collision. Furthermore, it must be taken into account that the megathrust shear force balances the effect of the gravitational force and determines the actual resistance to plate convergence both during subduction and collision. Here, we have shown that the reduction of submarine margin relief at the subduction-collision transition supports an increase in mountain height without an increase in the megathrust shear force. Thus, the build-up of topography during incipient collision does not necessarily increase the resistance to convergence and a decrease in convergence rates may be rather related to the positive buoyancy of continental crust. In addition, the deceleration of convergence may reflect other processes such as the viscous resistance of deforming mantle lithosphere (Clark, 2012) or in some occasions slab breakoff.

Finally, our force-balance considerations may be relevant also for the later tectonic evolution of orogens. For example, if the accretionary mass influx during protracted continental collision exceeds the erosional

mass efflux, the resulting crustal thickening may drive mountain heights above the elevation supported by the megathrust shear force (cf. Menant et al., 2020; Ruh, 2020). In this case the upper plate would eventually respond by extension, which counteracts crustal thickening and helps to maintain approximate force equilibrium (e.g., Lamb & Watts, 2010; Platt, 1986; Ring & Brandon, 2008). Examples of this may be the syn-collisional extensional detachment faulting in the central European Alps (Simplon fault) and the Himalayas (South Tibetan detachment), which took place when mountain heights where similar to or exceeded present-day elevations (Campani et al., 2012; Dielforder, 2017; Gébelin et al., 2013; Krsnik et al., 2020).

6. Conclusions

Based on analytical and finite-element force-balance models, we showed that the balance between gravitational forces and the megathrust shear force requires an increase in mountain height when the submarine relief is reduced at the subduction-collision transition. The reduction of submarine margin topography increases the deviatoric compression in the upper plate and allows mountain height to increase until the force-balance is re-established with a near-neutral stress state beneath the high mountains in the upper plate. The required increase in mountain height varies between several hundred meters to a few kilometers and is controlled mainly by the trench depth and the shear force magnitude. Changes in parameters like the megathrust dip angle or the wedge density play a minor role for the elevation increase.

The application of our results to natural subduction zones shows that the difference in mountain height between the onshore part of the Makran subduction zone and the adjoining Zagros collision zone can be explained by the margin-parallel difference in submarine relief and its effect on the force balance. For other active subduction zones worldwide, our study provides estimates of the mountain height increase that can be expected if these margins transitioned into collision zones without submarine relief. The estimated elevation increase varies from 0.5 km (Northern Cascadia) and 5.3 km (Java, Kamchatka). As the shear force for present-day collision zones is on average somewhat lower than for present-day subduction zones, our results can be regarded as a maximum estimate for the elevation increase. The decrease in F_s may result, for example, from syncollisional shallowing of the frictional-viscous-transition.

In conclusion, our study shows that force-balance analyses can provide quantitative constraints on the changes in mountain heights during the subduction-collision transition. The reduction in margin relief associated with the closure of the ocean basin causes deviatoric compression in the upper plate, which promotes tectonic shortening and mountain building. Our findings imply that mountain building during the subduction-collision transition can, in principle, occur without an increase in the megathrust shear force.

Data Availability Statement

All data used for the force balance analysis and for Figures 9 and 10 are available through Amante and Eakins (2009), Burg (2018), DeMets et al. (2010), Dielforder et al. (2020), Hayes et al. (2012, 2018), Hunter (2007), Penney et al. (2017), Tozer et al. (2019), and Vergés et al. (2011).

References

Abbott, L. D., Silver, E. A., Anderson, R. S., Smith, R., Ingle, J. C., Kling, S. A., et al. (1997). Measurement of tectonic surface uplift rate in a young collisional mountain belt. *Nature*, *385*, 501–507. https://doi.org/10.1038/385501a0

Abers, G. A., & McCaffrey, R. (1994). Active arc-continent collision: Earthquakes, gravity anomalies, and fault kinematics in the Huon-Finisterre collision zone, Papua New Guinea. *Tectonics*, *13*(2), 227–245. https://doi:10.1029/93TC02940

Ader, T., Avouac, J.-P., Liu-Zeng, J., Lyon-Caen, H., Bollinger, L., Galetzka, J., et al. (2012). Convergence rate across the Nepal Himalaya and interseismic coupling on the Main Himalayan Thrust: Implications for seismic hazard, *Journal of Geophysical Research*, *117*, B04403. https://doi.org/10.1029/2011JB009071

Alavi, M. (1994). Tectonics of the Zagros orogenic belt of Iran: new data and interpretations. *Tectonophysics*, *229*, 211–238. https://doi.org/10.1016/0040-1951(94)90030-2

Amante, C., & Eakins, B. W. (2009). *ETOPO1 1 arc-Minute global relief model NOAA Technical Memorandum*. National Centers for Environmental Information. https://doi.org/10.7289/V5C8276M

Baldwin, S. L., Fitzgerald, P. G. & Webb, L. E. (2012). Tectonics of the New Guinea Region. *Annual Review of Earth and Planetary Sciences*, *40*(1), 495–520. https://doi.org/10.1146/annurev-earth-040809-152540

Barber, D. E., Stockli, D. F., Horton, B. K., & Koshnaw, R. I. (2018). Cenozoic exhumation and foreland basin evolution of the Zagros orogen during the Arabia-Eurasia collision, western Iran. *Tectonics*, *37*, 4396–4420. https://doi.org/10.1029/2018TC005328

Botsyun, S., Sepulchre, P., Donnadieu, Y., Risi, C., Licht, A., & Rugenstein, J. K. C. (2019). Revised paleoaltimetry data show Tibetan Plateau elevation during the Eocene. *Science*, *363*, eaaq1436. https://doi.org/10.1126/science.aaq1436

Buiter, S. J. H., Govers, R., & Wortel, M. J. R. (2002). Two-dimensional simulation of surface deformation caused by slab detachment. *Tectonophysics*, *354*(3–4), 192–210. https://doi.org/10.1016/S0040-1951(02)00336-0

Burg, J.-P. (2018). Geology of the onshore Makran accretionary wedge: Synthesis and tectonic interpretation. *Earth-Science Reviews*, *185*, 1210–1231. https://doi.org/10.1016/j.earscirev.2018.09.011

Byrne, D. E., Sykes, L. R., & Davis, D. M. (1992). Great thrust earthquakes and aseismic slip along the plate boundary of the Makran Subduction Zone. *Journal of Geophysical Research*, *97*(B1), 449–478. https://doi.org/10.1029/91JB02165

Campani, M., Mulch, A., Kempf, O., Schlunegger, F., & Mancktelow, N. (2012). Miocene paleotopography of the Central Alps. *Earth and Planetary Science Letters*, *337–338*, 174–185. http://dx.doi.org/10.1016/j.epsl.2012.05.017

Carena, S., Suppe, J., & Kao, H. (2002). Active detachment of Taiwan illuminated by small earthquakes and its control of first-order topography. *Geology*, *30*(10), 935–938. https://doi.org/10.1130/0091-7613(2002)030<0935:ADOTIB>2.0.CO;2

Clark, M. K. (2012). Continental collision slowing due to viscous mantle lithosphere rather than topography. *Nature*, *483*, 74–77. https://doi.org/10.1038/nature10848

Clift, P., & Vannucchi, P. (2004). Controls on tectonic accretion versus erosion in subduction zones: Implications for the origin and recycling of the continental crust. *Reviews of Geophysics*, *42*, RG2001. https://doi.org/10.1029/2003RG000127

Cloos, M. (1993). Lithospheric buoyancy and collisional orogenesis – Subduction of oceanic plateaus, continental margins, island arcs, spreading ridges, and seamounts. The *Geological Society of America Bulletin*, *105*, 715–737. https://doi.org/10.1130/0016-7606(1993)105<0715:LBACOS>2.3.CO;2

Cloos, M., Sapiie, B., van Ufford, A. Q., Weiland, R. J., Warren, P. Q., & McMahon, T. P. (2005). *Collisional delamination in new Guinea: The geotectonics of subducting slab breakoff*. Boulder, CO: Geological Society of America. https://doi.org/10.1130/SPE400

Copley, A., Avouac, J.-P., & Royer, J.-Y. (2010). India-Asia collision and the Cenozoic slowdown of the Indian plate: Implications for the forces driving plate motions. *Journal of Geophysical Research*, *115*, B03410. https://doi.org/10.1029/2009JB006634

Dahlen, F. A. (1990). Critical taper model of fold-and-thrust belts and accretionary wedges. *Annual Review of Earth and Planetary Sciences*, *18*(1), 55–99.

Dal Zilio, L., van Dinther, Y., Gerya, T., & Avouac, J.-P. (2019). Bimodal seismicity in the Himalaya controlled by fault friction and geometry. *Nature Communications*, *10*(48). https://doi.org/10.1038/s41467-018-07874-8

Dalmayrac, B., & Molnar, P. (1981). Parallel thrust and normal faulting in Peru and constraints on the state of stress. *Earth and Planetary Science Letters*, *55*, 473–481. https://doi.org/10.1016/0012-821X(81)90174-6

Davis, D., Suppe, J., & Dahlen, F. A. (1983). Mechanics of fold-and-thrust belts and accretionary wedges. *Journal of Geophysical Research*, *88*(B2), 1153–1172. https://doi.org/10.1029/JB088iB02p01153

DeMets, C., Gordon, R. G., & Argus, D. F. (2010). Geologically current plate motions. *Geophysical Journal International*, *181*(1), 1–80. https://doi.org/10.1111/j.1365-246X.2009.04491.x

Dielforder, A. (2017). Constraining the strength of megathrust from fault geometries and application to the Alpine collision zone. *Earth and Planetary Science Letters*, *474*, 49–58. https://doi.org/10.1016/j.epsl.2017.06.021

Dielforder, A., Berger, A., & Herwegh, M. (2016). The accretion of foreland basin sediments during early stages of continental collision and similarities to accretionary wedge tectonics. *Tectonics*, *35*, 2216– 2238. https://doi:10.1002/2015TC004101

Dielforder, A., Hetzel, R., & Oncken, O. (2020). Megathrust shear force controls mountain height at convergent plate margins. *Nature*, *582*, 225–229. https://doi.org/10.1038/s41586-020-2340-7

Dielforder, A., Vollstaedt, H., Vennemann, T., Berger, A., & Herwegh, M. (2015). Linking megathrust earthquakes to brittle deformation in a fossil accretionary complex. *Nature Communications*, *6*, 7504. https://doi.org/10.1038/ncomms8504

Ding, L., Spicer, R. A., Yang, J., Xu, Q., Cai, F., Li, S., et al. (2017). Quantifying the rise of the Himalaya orogen and implications for the South Asian monsoon. *Geology*, *45*(3), 215–218. https://doi.org/10.1130/G38583.1

Duretz, T., Gerya, T. V., May, D. A. (2011). Numerical modeling of spontaneous slab breakoff and subsequent topographic response. *Tectonophysics*, *502* (1–2), 244–256. https://doi.org/10.1016/j.tecto.2010.05.024

Faccenna, C., Oncken, O., Holt, A. F., & Becker, T. W. (2017). Initiation of the Andean orogeny by lower mantle subduction. *Earth and Planetary Science Letters*, *463*, 189–201. https://doi.org/10.1016/j.epsl.2017.01.041

Fagereng, Å., & Biggs, J. (2019). New perspectives on 'geological strain rates' calculated from both naturally deformed and actively deforming rocks. *Journal of Structural Geology*, *125*, 100–110. https://doi.org/10.1016/j.jsg.2018.10.004

Ford, M., Duchêne, S., Gasquet, D., & Vanderhaeghe, O. (2006). Two-phase orogenic convergence in the external SW Alps. *Journal of the Geological Society*, *163*, 815–826. https://doi.org/10.1144/0016-76492005-034

François, T., Agard, P., Bernet, M., Meyer, B., Chung, S.-L., Zarrinkoub, M. H., et al. (2014). Cenozoic exhumation of the internal Zagros: first constraints from low-temperature thermochronology and implications for the build-up of the Iranian plateau. *Lithos*, *206–207*, 100–112. https://doi.org/10.1016/j.lithos.2014.07.021

Fruehn, J., White, R. S., & Minshull, T. A. (1997). Internal deformation and compaction of the Makran accretionary wedge. *Terra Nova*, *9*(3), 101–104. https://doi.org/10.1046/j.1365-3121.1997.d01-13.x

Gao, R., Lu, Z., Klemperer, S. L., Wang, H., Dong, S., Li, W., Li, H.. (2016). Crustal-scale duplexing beneath the Yarlung Zangbo suture in the western Himalayas. *Nature Geoscience*, *9*, 555–560. https://doi.org/10.1038/ngeo2730

Gao, X., & Wang, K. (2014). Strength of stick-slip and creeping subduction megathrusts from heat flow observations. *Science*, *345*, 1038–1041. https://doi.org/10.1126/science.1255487

Garzic, E. L., Vergés, J., Sapin, F., Saura, E., Meresse, F., & Ringenbach, J. C. (2019). Evolution of the NW Zagros Fold-and-Thrust Belt in Kurdistan Region of Iraq from balanced and restored crustal-scale sections and forward modeling. *Journal of Structural Geology*, *124*, 51–69. https://doi.org/10.1016/j.jsg.2019.04.006

Gébelin, A., Mulch, A., Teyssier, C., Jessup, M. J., Law, R. D., & Brunel, M. (2013). The Miocene elevation of Mount Everest. *Geology*, *41*(7), 799–802. https://doi.org/10.1130/G34331.1

Hampel, A., Lüke, J., Krause, T., & Hetzel, R. (2019). Finite-element modeling of glacial isostatic adjustment (GIA): Use of elastic foundations at material boundaries versus the geometrically non-linear formulation. *Computers & Geosciences*, *122*, 1–14. https://doi.org/10.1016/j.cageo.2018.08.002

Hardebeck, J. L., & Okada, T. (2018). Temporal stress changes caused by earthquakes: A review. *Journal of Geophysical Research*, *123*, 1350–1365. https://doi.org/10.1002/2017JB014617

Hayes, G. P., Moore, G. L., Portner, D. E., Hearne, H. F., Furtney, M., & Smoczyk, G. M. (2018). Slab2, a comprehensive subduction zone geometry model. *Science*, *362*, 58–61. https://doi.org/10.1126/science.aat4723

Hayes, G. P., Wald, D. J., & Johnson, R. L. (2012). Slab1.0: A three-dimensional model of global subduction zone geometry. *Journal of Geophysical Research*, *117*, B013012. https://doi.org/10.1029/2011JB008524

Heuret, A., Lallemand, S., Funiciello, F., Piromallo, C., & Faccenna, C. (2011). Physical characteristics of subduction interface type seismogenic zones revisited. *Geochemistry, Geophysics, Geosystems*, *12*, Q01004. https://doi.org/10.1029/2010GC003230

Hirth, G., Teyssier, C., Dunlap, W. J. (2001). An evaluation of quartzite flow laws based on comparisons between experimentally and naturally deformed rocks. *International Journal of Earth Sciences*, *90*, 77–87. https://doi.org/10.1007/s005310000152

Hunter, J. D. (2007). Matplotlib: a 2D graphics environment. *Computing in Science & Engineering*, *9*, 90–95. https://doi.org/10.1109/MCSE.2007.55

Husson, L. & Ricard, Y. (2004). Stress balance above subduction: application to the Andes. *Earth and Planetary Science Letters*, *222*(3–4), 1037–1050. https://doi.org/10.1016/j.epsl.2004.03.041

Kapp, P., & DeCelles, P. G. (2019). Mesozoic-Cenozoic geological evolution of the Himalayan-Tibetan orogen and working hypotheses. *American Journal of Science*, *319*, 159–254. https://doi.org/10.2475/03.2019.01

Koshnaw, R. I., Stockli, D. F., & Schlunegger, F. (2018). Timing of the Arabia-Eurasia continental collision—Evidence from detrital zircon U-Pb geochronology of the Red Bed Series strata of the northwest Zagros hinterland, Kurdistan region of Iraq. *Geology*, *47*(1), 47–50. https://doi.org/10.1130/G45499.1

Krsnik, E., Methner, K., Löffler, N., Kempf, O., Fiebig, J., & Mulch, A. (2020). New paleoelevation constraints on the Mid-Miocene Central Alps. *Paper presented at EGU General Assembly 2020, Online.* https://doi.org/10.5194/egusphere-egu2020-10060

Lamb, S. (2006). Shear stresses on megathrusts: Implications for mountain building behind subduction zones. *Journal of Geophysical Research*, *111*, B07401. https://doi.org/10.1029/2005JB003916

Lamb, S., & Davis, P. (2003). Cenozoic climate change as a possible cause for the rise of the Andes. *Nature*, *425*, 792–797. https://doi.org/10.1038/nature02049

Lamb, S., & Watts, A. (2010). The origin of mountains – implications for the behavior of Earth's lithosphere. *Current Science*, *99*(12), 1699–1718.

Lee, Y.-H., Chen, C.-C., Liu, T.-K., Ho, H.-C., Lu, H.-Y., & Lo, W. (2006). Mountain building mechanisms in the Southern Central Range of the Taiwan Orogenic Belt – From accretionary wedge deformation to arc–continental collision. *Earth and Planetary Science Letters*, *252*(3–4), 413–422. https://doi.org/10.1016/j.epsl.2006.09.047

Luo, G., & Liu, M. (2009). Why short-term crustal shortening leads to mountain building in the Andes, but not in Cascadia? *Geophysical Research Letters*, *36*, L08301. https://doi.org/10.1029/2009GL037347

Maxelon, M., & Mancktelow, N. S. (2005). Three-dimensional geometry and tectonostratigraphy of the Pennine zone, Central Alps, Switzerland and Northern Italy. *Earth-Science Reviews*, *71*, 171–227. http://dx.doi.org/10.1016/j.earscirev.2005.01.003

McIntosh, K., van Avendonk, H., Lavier, L., Lester, W. R., Eakin, D., Wu, F., et al. (2013). Inversion of a hyper-extended rifted margin in the southern Central Range of Taiwan. *Geology*, *41*(8), 871–874. https://doi.org/10.1130/G34402.1

McKenzie, D. P. (1969). Speculations on the consequences and causes of plate motions*. *Geophysical Journal of the Royal Astronomical Society*, *18*, 1–32. https://doi.org/10.1111/j.1365-246X.1969.tb00259.x

McQuarrie, N., & van Hinsbergen, D. J. J. (2013). Retrodeforming the Arabia-Eurasia collision zone: Age of collision versus magnitude of continental subduction. *Geology*, *41*(3), 315–318. https://doi.org/10.1130/G33591.1

Menant, A., Angiboust, S., Gerya, T., Lacassin, R., Simoes, M., Grandin, R. (2020). Transient stripping of subducting slabs controls periodic forearc uplift. *Nature Communications*, *11*:1823. https://doi.org/10.1038/s41467-020-15580-7

Mohammad, Y. O., & Karim, K. H. (2019). Timing of the Arabia-Eurasia continental collision—Evidence from detrital zircon U-Pb geochronology of the Red Bed Series strata of the northwest Zagros hinterland, Kurdistan region of Iraq: COMMENT. *Geology*, *47*(8), e471. https://doi.org/10.1130/G46315C.1

Molinaro, M., Leturmy, P., Guezou, J. -C., Frizon de Lamotte, D., & Eshraghi, S. A. (2005). The structure and kinematics of the southeastern Zagros fold-thrust belt, Iran: From thin-skinned to thick-skinned tectonics, *Tectonics*, *24*, TC3007. https://doi.org/10.1029/2004TC001633

Molnar, P., & Lyon-Caen, H. (1988). Some simple physical aspects of the support, structure, and evolution of mountain belts. In S. P. Clark Jr, B. C. Burchfiel, & J. Suppe (Eds.), Processes in continental lithospheric deformation (Vol. 281, pp. 179–208). Boulder, CO: Geological Society of America.

Molnar, P., & Stock, J. M. (2009). Slowing of India's convergence with Eurasia since 20 Ma and its implications for Tibetan mantle dynamics. *Tectonics*, *28*, TC3001. https://doi.org/10.1029/2008TC002271

Montgomery, D. R., & Brandon, M. T. (2002). Topographic controls on erosion rates in tectonically active mountain ranges. *Earth and Planetary Science Letters*, *201*, 481–489. https://doi.org/10.1016/S0012-821X(02)00725-2

Moores, E. M., Twiss, R. J. (1995). *Tectonics*. New York, NY: W. H. Freeman.

Mouthereau, F., Lacombe, O., & Vergés, J. (2012). Building the Zagros collisional orogen: Timing, strain distribution and the dynamics of Arabia/Eurasia plate convergence. *Tectonophysics*, *532–535*, 27–60. https://doi.org/10.1016/j.tecto.2012.01.022

Norabuena, E. O., Dixon, T. H., Stein, S., & Harrison, C. G. A. (1999). Decelerating Nazca-South America and Nazca-Pacific plate motions. *Geophysical Research Letters*, *26*, 3405–3408. https://doi.org/10.1029/1999GL005394

Oncken, O., von Winterfeld, C., & Dittmar, U. (1999). Accretion of a rifted passive margin: The Late Paleozoic Rhenohercynian fold and thrust belt (Middle European Variscides), *Tectonics*, *18*(1), 75– 91, https://doi.org/10.1029/98TC02763

Penney, C., Tavakoli, F., Saadat, A., Nankali, H. R., Sedigihi, M., Khorrami, F., et al., (2017). Megathrust and accretionary wedge properties and behavior in the Makran subduction zone. *Geophysical Journal International*, *209*(3), 1800–1830. https://doi.org/10.1093/gji/ggx126

Pfiffner, A. O. (1986). Evolution of the north Alpine foreland basin in the central Alps. In P. A. Allen, P. Homewood (Eds.), Foreland basins, Special Publications of the International association of Sedimentologists (Vol. 8, 219–228). Oxford: Blackwell Scientific.

Platt, J. P. (1986). Dynamics of orogenic wedges and the uplift of high-pressure metamorphic rocks. The *Geological Society of America Bulletin*, *97*, 1037–1053. https://doi.org/10.1130/0016-7606(1986)97<1037:DOOWAT>2.0.CO;2

Platt, J. P., Leggett, J. K., Young, J., Raza, H., & Alam, S. (1985). Large-scale sediment underplating in the Makran accretionary prism. *Geology*, *13*(7), 507–511. https://doi.org/10.1130/0091-7613(1985)13<507:LSUITM>2.0.CO;2

Ranalli, G., Pellegrini, R., & D'Offizi, S. (2000). Time dependence of negative buoyancy and the subduction of continental lithosphere. *Journal of Geodynamics*, *30*(5), 539–555. https://doi.org/10.1016/S0264-3707(00)00011-9

Regard, V., Faccenna, C., Martinod, J., Bellier, O., & Thomas, J.-C. (2003). From subduction to collision: Control of deep processes on the evolution of convergent plate boundary. *Journal of Geophysical Research*, *108*(B4), 2208. https://doi.org/10.1029/2002JB001943

Ring, U., & Brandon, M. T. (2008). Exhumation settings, Part I: Relatively simple cases. *International Geology Review*, *50*, 97–120, https://doi.org/10.2747/0020-6814.50.2.97

Roe, G. H., Stolar, D. B. & Willett, S. D. (2006). Response of a steady-state critical wedge orogen to changes in climate and tectonic forcing. In S. D. Willett, N. Hovius, M. T. Brandon, D. M. Fisher (Eds.), Tectonics, climate, and landscape evolution, GSA Special Publications (Vol. 398, 227–239). Boulder CO: Geological Society of America.

Rosenberg, C. L., & Berger, A. (2009). On the causes and modes of exhumation and lateral growth of the Alps. *Tectonics*, *28*, TC6001. https://doi.org/10.1029/2008TC002442

Rowley, D. B., & Currie, B. S. (2006). Paleo-altimetry of the late Eocene to Miocene Lunpola basin, central Tibet. *Nature*, *439*, 667–681. https://doi.org/10.1038/nature04506

Ruh, J. B. (2020), Numerical modeling of tectonic underplating in accretionary wedge systems. *Geosphere*, *16*(6), 1385– 1407. https://doi.org/10.1130/GES02273.1

Saylor, J. E., Quade, J., Dellman, D. L., DeCelles, P. G., Kapp, P. A., & Ding, L. (2009). The late Miocene through present paleoelevation history of southwestern Tibet. *American Journal of Science*, *309*, 1–42, https://doi.org/10.2475/01.2009.01

Scheiber, T., Pfiffner, A. O., & Schreurs, G. (2012). Strain accumulation during basal accretion in continental collision – A case study from the Suretta nappe (eastern Swiss Alps). *Tectonophysics*, *579*, 56–73. https://doi.org/10.1016/j.tecto.2012.03.009

Schlunegger, F., & Kissling, E. (2015). Slab rollback orogeny in the Alps and evolution of the Swiss Molasse basin. *Nature Communications*, *6*:8605. https://doi.org/10.1038/ncomms9605

Schwanghart, W., & Scherler, D. (2014). TopoToolbox 2 – MATLAB-based software for topographic analysis and modeling in Earth surface sciences. *Earth Surface Dynamics*, *2*, 1–7. https://doi.org/10.5194/esurf-2-1-2014

Seno, T. (2009). Determination of the pore fluid pressure ratio at seismogenic megathrusts in subduction zones: Implications for strength of asperities and Andean-type mountain building, *Journal of Geophysical Research*, *114*, B05405. https://doi.org/10.1029/2008JB005889

Seton, M., Muller, R. D., Zahirovic, S., Gaina, C., Torsvik, T. H., Shephard, G., et al. (2012). Global continental and ocean basin reconstructions since 200 Ma. *Earth-Science Reviews*, *113*(3–4), 212–270. http://dx.doi.org/10.1016/j.earscirev.2012.03.002

Sinclair, H. D.. (1997). Flysch to Molasse transition in peripheral foreland basins: The role of the passive margin versus slab breakoff. *Geology*, *25*(12), 1123–1126. https://doi.org/10.1130/0091-7613(1997)025<1123:FTMTIP>2.3.CO;2

Sinclair, H. D., & Allen, P. A. (1992). Vertical versus horizontal motions in the Alpine orogenic wedge: stratigraphic response in the foreland basin. *Basin Research*, *4*, 215–232. https://doi.org/10.1111/j.1365-2117.1992.tb00046.x

Sippl, C., Schurr, B., Asch, G., & Kummerow, J. (2018). Seismicity structure of the northern Chile forearc from >100,000 double-difference relocated hypocenters. *Journal of Geophysical Research*, *123*, 4063–4087. https://doi.org/10.1002/2017JB015384

Smith, G. L., McNeill, L. C., Wang, K., He, J., & Henstock, T. J. (2013). Thermal structure and megathrust seismogenic potential of the Makran subduction zone, *Geophysical Research Letters*, *40*, 1528–1533. https://doi.org/10.1002/grl.50374

Song, X.-Y., Spicer, R. A., Yang, J., Yao, Y.-F., Li, C.-S. (2010). Pollen evidence for an Eocene to Miocene elevation of central southern Tibet predating the rise of the High Himalaya. *Palaeogeography, Palaeoclimatology, Palaeoecology*, *297*(1), 159–168. https://doi.org/10.1016/j.palaeo.2010.07.025

Spicer, R. A., Farnsworth, A., & Su, T. (2020). Cenozoic topography, monsoons and biodiversity conservation within the Tibetan Region: An evolving story. *Plant Diversity, 42*, 229–254. https://doi.org/10.1016/j.pld.2020.06.011

Stipp, M., Stünitz, H., Heilbronner, R., & Schmid, S. M. (2002). The eastern Tonale fault zone: a 'natural laboratory' for crystal plastic deformation of quartz over a temperature range from 250 to 700°C. *Journal of Structural Geology*, *24*, 1861–1884. https://doi.org/10.1016/S0191-8141(02)00035-4

Stolar, D., Roe, G., & Willett, S. (2007). Controls on the patterns of topography and erosion rate in a critical orogen. *Journal of Geophysical Research*, *112*, F04002. https://doi.org/10.1029/2006JF000713

Stolar, D. B., Willett, S. D., & Roe, G. H. (2006). Climate and tectonic forcing of a critical orogen. In S. D. Willett, N. Hovius, M. T. Brandon, D. M. Fisher (Eds.), Tectonics, Climate, and Landscape evolution, GSA Special Publications (Vol. 398, pp. 227–239), Boulder, CO: Geological Society of America.

Suppe, J. (2007). Absolute fault and crustal strength from wedge tapers. *Geology*, *35*(12), 1127–1130. https://doi.org/10.1130/G24053A.1

Tate, G. W., McQuarrie, N., van Hinsbergen, D. J. J., Bakker, R. R., Harris, R., & Jiang, H. (2015). Australia going down under: Quantifying continental subduction during arc-continent accretion in Timor-Leste. *Geosphere*, *11*(6): 1860–1883. https://doi.org/10.1130/GES01144.1

Tavani, S., Parente, M., Puzone, F., Corradetti, A., Gharabeigli, G., Valinejad, M., et al. (2018). The seismogenic fault system of the 2017 Mw 7.3 Iran–Iraq earthquake: constraints from surface and subsurface data, cross-section balancing, and restoration. *Solid Earth*, *9*, 821–831. https://doi.org/10.5194/se-9-821-2018

Tozer, B., Sandwell, D. T., Smith, W. H. F., Olson, C., Beale, J. R., & Wessel, P. (2019). Global bathymetry and topography at 15 arc sec: SRTM15+. *Earth and Space Science*, *6*, 1847–1864. https://doi.org/10.1029/2019EA000658

van den Beukel, J.. (1992). Some thermomechanical aspects of the subduction of continental lithosphere. *Tectonics*, *11*(2), 319–329. https://doi.org/10.1029/91TC01039

Vergés, J., Saura, E., Casciello, E., Fernàndez, M., Villaseñor, A., Jiménez-Munt, I., & García-Castellanos, D. (2011). Crustal-scale cross-sections across the NW Zagros belt: Implications for the Arabian margin reconstruction. *Geological Magazine*, *148*(5–6), 739–761. https://doi:10.1017/S0016756811000331

Vernant, Ph., Nilforoushan, F., Hatzfeld, D., Abbassi, M. R., Vigny, C., Masson, F., et al. (2004). Present-day crustal deformation and plate kinematics in the Middle East constrained by GPS measurements in Iran and northern Oman. *Geophysical Journal International*, *157*(1), 381–398. https://doi.org/10.1111/j.1365-246X.2004.02222.x

Wada, I., & Wang, K. (2009). Common depth of slab-mantle decoupling: reconciling diversity and uniformity of subduction zones. *Geochemistry, Geophysics, Geosystems*, *10*, Q10009. https://doi.org/10.1029/2009GC002570

Wang, K. (2000). Stress–strain 'paradox', plate coupling, and forearc seismicity at the Cascadia and Nankai subduction zones. *Tectonophysics*, *319*(4), 321–338. https://doi.org/10.1016/S0040-1951(99)00301-7

Wang, K., Brown, L., Hu, Y., Yoshida, K., He, J., & Sun, T. (2019). Stable forearc stressed by a weak megathrust: Mechanical and geodynamic implications of stress changes caused by the M = 9 Tohoku-Oki earthquake. *Journal of Geophysical Research*, *124*. 6179– 6194. https://doi.org/10.1029/2018JB017043

Wang, K., & He, J. (1999). Mechanics of low stress forearcs: Nankai and Cascadia. *Journal of Geophysical Research*, *104*(B7), 15191–15205. https://doi.org/10.1029/1999JB900103

Whipple, K. X., & Meade, B. J. (2006). Orogen response to changes in climatic and tectonic forcing. *Earth and Planetary Science Letters, 243*, 218–228. https://doi.org/10.1016/j.epsl.2005.12.022

Wiederkehr, M., Bousquet, R., Schmid, S. M., & Berger, A. (2008). From subduction to collision: Thermal overprint of HP/LT meta-sediments in the north-eastern Lepontine Dome (Swiss Alps) and consequences regarding the tectono-metamorphic evolution of the Alpine orogenic wedge. *Swiss Journal of Geoscience*, *101*, 127–155. https://doi.org/10.1007/s00015-008-1289-6

Willett, S. D., & Brandon, M. T. (2002). On steady states in mountain belts. *Geology*, *30*, 175–178. https://doi.org/10.1130/0091-7613(2002)030<0175:OSSIMB>2.0.CO;2

Williams, C. A., Connors, C., Dahlen, F. A., Price, E. J., and Suppe, J. (1994), Effect of the brittle–ductile transition on the topography of compressive mountain belts on Earth and Venus, *Journal of Geophysical Research*, *99*(B10), 19947–19974, https://doi.org/10.1029/94JB01407

Wimpenny, S., Benavente, C., Copley, A., Garcia, B., Rosell, L., O'Kane, A., & Aguirre, E. (2020). Observations and dynamical implications of active normal faulting in South Peru. *Geophysical Journal International*, *222*, 27–53. https://doi.org/10.1093/gji/ggaa144

Wright, T. J., Elliot, J. R., Wang, H., Ryder, I. (2013). Earthquake deformation and the Moho: implications for the rheology of continental lithosphere. *Tectonophysics*, *609*, 504–523. https://doi.org/10.1016/j.tecto.2013.07.029

Xu, Q., Ding, L., Hetzel, R., Yue, Y., & Rades, E. F. (2015). Low elevation of the northern Lhasa terrane in the Eocene: implications for relief development in south Tibet. *Terra Nova*, *27*, 458–466. https://doi.org/10.1111/ter.12180

Xu, Q., Ding, L., Spice, R. A., Liu, X., Li, S., & Wang, H. (2018). Stable isotopes reveal southward growth of the Himalayan-Tibetan Plateau since the Paleocene. *Gondwana Research*, *54*, 50–61. https://doi.org/10.1016/j.gr.2017.10.005